science.sciencemag.org/content/371/6529/595/suppl/DC1

Supplementary Materials for

Fecal microbiota transplant overcomes resistance to anti–PD-1 therapy in melanoma patients

Diwakar Davar*, Amiran K. Dzutsev*, John A. McCulloch, Richard R. Rodrigues, Joe-Marc Chauvin, Robert M. Morrison, Richelle N. Deblasio, Carmine Menna, Quanquan Ding, Ornella Pagliano, Bochra Zidi, Shuowen Zhang, Jonathan H. Badger, Marie Vetizou, Alicia M. Cole, Miriam R. Fernandes, Stephanie Prescott, Raquel G. F. Costa, Ascharya K. Balaji, Andrey Morgun, Ivan Vujkovic-Cvijin, Hong Wang, Amir A. Borhani, Marc B. Schwartz, Howard M. Dubner, Scarlett J. Ernst, Amy Rose, Yana G. Najjar, Yasmine Belkaid, John M. Kirkwood, Giorgio Trinchieri†‡, Hassane M. Zarour†‡

*These authors contributed equally to this work.
†These authors contributed equally to this work.
‡Corresponding author. Email: zarourhm@upmc.edu (H.M.Z.); trinchig@mail.nih.gov (G.T.)

Published 5 February 2021, *Science* **371**, 595 (2021)
DOI: 10.1126/science.abf3363

This PDF file includes:

Other Supporting Online Material for this manuscript includes the following:
(available at science.sciencemag.org/content/371/6529/595/suppl/DC1)

MDAR Reproducibility Checklist (.pdf)

Materials and Methods

Clinical Trial Design: Summary, Recipient Eligibility Criteria, Donor Selection Criteria, Donor/Recipient Seromatching, and Study Conduct

Summary: This was a phase II Simon's two-stage single-center study of concurrent fecal microbiota transplantation (FMT) with pembrolizumab in patients with programmed cell death protein 1 (PD-1)-refractory melanoma. The primary objective was to investigate whether a combination of single PD-1 responder (R)-derived FMT with pembrolizumab can convert PD-1 non-responders (NRs) to Rs. Secondary and exploratory objectives were to determine the effect of FMT administration on the composition and function of T cells and innate/adaptive immune system subsets and the gut microbiota, respectively.

Recipient Eligibility Criteria: Recipient eligibility was based upon prior exposure to PD-1 inhibitor therapy and response at first (or subsequent) restaging scan(s). Patients must have received a minimum of two cycles of anti-PD-1 to be considered eligible. Patients who received either nivolumab or pembrolizumab as a single agent or in combination with other standard or investigational agent(s) were eligible. PD-1-refractory disease was defined as progressive disease (PD) at first (or subsequent) radiographic evaluation while receiving PD-1 inhibitor treatment as assessed by response evaluation criteria in solid tumors (RECIST) v1.1 (*15*). Patients with stable disease (SD) as their best response were eligible, but patients with complete response (CR) or partial response (PR) as their best response were ineligible (*16*). Other eligibility criteria included absence of active central nervous system (CNS) disease, presence of disease amenable to biopsy, and lack of contraindication to FMT.

Donor Selection Criteria: Candidate donors were patients with advanced unresectable stage IIIB–D or metastatic melanoma treated with anti-PD-1 (nivolumab or pembrolizumab) with ongoing durable PR or CR. Median duration of follow up was ≥24 months (for partial Rs) or ≥12 months (for complete Rs). Other eligibility criteria included willingness to complete a donor-specific questionnaire and undergo donor-specific serologic testing to evaluate infectious agents. Donor-specific exclusion criteria included history of antibiotic treatment during the 1 month preceding donation; history of intrinsic gastrointestinal illnesses including inflammatory bowel disease, irritable bowel syndrome, chronic diarrheal disorder (celiac disease), active primary gastrointestinal malignancies, or major gastrointestinal surgical procedures; history of symptomatic autoimmune illness; history of documented chronic pain syndromes (fibromyalgia, chronic fatigue) or neurologic, neurodevelopmental disorders; and history of metabolic syndrome, obesity (body mass index > 35), or moderate-to-severe malnutrition (as assessed clinically). Only patients deemed suitable by a screening questionnaire and serological/stool/nasal swab tests were deemed suitable to donate stool samples to create FMTs. While on study, candidate FMT donors underwent systematic retesting before FMT sampling to minimize the possibility of transmitting infectious agents (**Fig. S2**).

Donor/Recipient Seromatching and Study Conduct: Potential recipients underwent a screening evaluation consisting of imaging (including CNS if clinically suspected), tumor biopsy, and serological/stool studies to confirm suitability for FMT administration. Donors or recipients who tested positive for infections with latent potential (human immunodeficiency virus, hepatitis B/C, human T-cell lymphotropic virus type 1 [HTLV-1], HTLV-2, strongyloides, syphilis) and/or had evidence of multi-drug resistant organisms such as vancomycin-resistant *Enterococcus*, carbapenem-resistant *Enterobacteriaceae*, and extended spectrum beta-lactamase were ineligible. Candidate recipients and donors were sero-matched for cytomegalovirus, Epstein-Barr virus, herpes simplex virus 1/2, John Cunningham virus, human herpesvirus 6, and methicillin-resistant *Staphylococcus aureus*.

Eligible patients received FMT endoscopically with one cycle of pembrolizumab (±3 days) followed by three additional cycles of pembrolizumab (cycles 2–4), depending on which restaging computed tomography (CT) scans were performed. Patients with SD and/or responding disease continued to receive pembrolizumab on study until disease progression or intolerable toxicity for up to 2 years from FMT administration (35 cycles total). Response was first assessed after four cycles of pembrolizumab and every 12 weeks thereafter based on RECIST 1.1 (*15*). Because tumor pseudo-progression is a well-recognized consequence of PD-1-based immunotherapies

and use of FMT as a therapeutic agent in cancer is highly novel, PD was confirmed if observed on two consecutive assessments of response at least 4 weeks apart, during which time pembrolizumab was continued.

DNA Extraction and Shotgun Metagenomic Sequencing and Analysis

Total metagenomic DNA was extracted from stool samples using the MO BIO PowerSoil DNA Isolation Kit (MO BIO Laboratories, Carlsbad, CA, USA) and Epmotion 5075 liquid handling robot (Eppendorf). The DNA library was prepared using the Nextera DNA Flex Library Prep Kit, quantified using Qbit, and sequenced on the NovaSeq System (Illumina, Inc, San Diego, CA, USA) using the 2×150 base pair (bp) paired-end protocol.

For each shotgun metagenomic sample, after quality trimming and adapter clipping with Trimmomatic 0.36 (*44*), raw reads were aligned against the human genome to filter out human reads with Bowtie2 v2.3.2 (*45*). Leftover (non-host) reads were assembled using MEGAHIT v1.2.9 (*46*). Resulting assembly contigs <500 bp were discarded. For the 216 samples sequenced, the mean number of non-human bp used for assembly into contigs was 2.73 Gbp ± 0.78 Gbp, yielding a mean assembly rate of 78.27% ± 7.48%.

Contigs were classified taxonomically by k-mer analysis using Kraken2 (*47*), with a custom 96-Gb Kraken2 database built with draft and complete genomes of all bacteria, archaea, fungi, viruses, and protozoa available in the NCBI GenBank in April 2020, in addition to human and mouse genomes. Contigs were annotated ab initio with Prokka v1.14.6 (*48*). Then reads used for assembly were aligned back to the assembly contigs to gauge sequencing depth of each contig. Unassembled reads were retrieved and classified one by one using Kraken2 on the same database. Taxonomic classifications were expressed as the last known taxon (LKT), which is the lowest unambiguous classification known for the query sequence, using Kraken's confidence scoring threshold of 5e-06 (using the –confidence parameter).

In each sample, relative abundance for each LKT was calculated by dividing the number of bp covering all contigs and unassembled reads classified as that LKT by the total number of host-filtered bp used for assembly in that sample. This ratio was multiplied by 10^6 to yield relative abundance in parts per million (PPM).

For beta analysis, ordination plots were done using t-distributed stochastic neighbor embedding (t-SNE) implemented via the uwot package in R (https://github.com/jlmelville/uwot) and the ggplot2 library. Heatmaps were drawn using the ComplexHeatmap package for R (*49*).

All codes used for shotgun sequencing analysis can be found within the in-house JAMS_BW package, version 1.5.5, publicly available on GitHub (https://github.com/johnmcculloch/JAMS_BW).

Meta-analysis of microbiome associated with the response was done as follows. Individual Rs were first analyzed using the non-parametric *t*-test. Then p-values and ratios were combined using Fisher's method and R package meta (https://github.com/guido-s/meta). Resultant data were visualized using the cladogram feature from package LEfSe (*50*).

Assessing Reactivity of Recipient Sera to Donor Fecal Bacteria by IgG Flow Cytometry

Evaluation of IgG Response in Recipient Sera to Donor Fecal Bacteria: Donor fecal bacteria were separated from particulates by centrifugation at 50g for 1 minute. Fecal bacterial suspensions were normalized to equivalent OD600 and were incubated with recipient sera at 1:200 dilutions in phosphate buffered saline with 1% bovine serum albumin for 30 minutes. Suspensions were washed and stained with anti-IgG (PE, Miltenyi clone Is11-3B2.2.3; 1:50 dilution) and SYTO-62 (staining bacterial cells in APC; 1:1,000 dilution) for 15 minutes at 4^0C. Suspensions were washed, fixed in 2% paraformaldehyde for 15 minutes, and analyzed on a Becton Dickinson Fortessa flow cytometer.

IgG Flow Cytometry Data Analysis: Change in IgG positivity of donor fecal bacteria for each FMT recipient was calculated in relation to the first FMT recipient serum sample available (baseline) compared to the subsequent

two time points up to 50 days later. Analysis was limited to the subsequent two time points post-baseline because later time points were not equally available for all subjects due to mortality. Percent IgG-positive donor fecal bacteria were assessed by setting IgG-positive gates for negative control (no serum) donor bacterial suspension samples to 0.5% positivity. Area-under-the-curve (AUC, R package 'DescTools') for the change in percent IgG-positive donor bacteria was calculated adjusting all recipient time points relative to the baseline time point by subtraction, with the baseline IgG-positive proportion being thus set to zero. Student's T-test was performed to test differences in IgG positivity of donor fecal bacteria over time as quantified by AUC.

Multiparameter Flow Cytometry and Unsupervised Analysis of Peripheral Blood Mononuclear Cells

Cryopreserved peripheral blood mononuclear cells (PBMCs) from patients undergoing combined anti-PD-1 and FMT treatment at three time points (days 0, 21, and 42) were thawed, washed, and resuspended in complete Iscove's Dulbecco's Modified Eagle Medium (10% human serum, 1% penicillin and streptomycin, 1% L-glutamine, 1% Hepes, and 1% non-essential amino acids). Cells were equally divided into five staining panels (depicted below). Cells in each panel were labeled for viability with Zombie NIR (BioLegend, San Diego, CA, USA) (15 min, room temperature) and stained with 29-color panels of anti-human monoclonal antibodies against surface (20 min, 4°C) and intracellular markers (30 min, 4°C). Cells were permeabilized in 2% hypertonic formaldehyde for 20 min at room temperature, followed by 1X BD perm/wash buffer (BD Biosciences, Franklin Lakes, NJ, USA), per the manufacturer's protocol. Each panel included a set of markers of interest and a common core of lineage markers. The antibodies used are outlined in the table below and include: CD1a and CXCR-5 BUV395, CD16 BUV496, CD123 and CD25 BUV563, CD56 BUV661, CD19 and CD8 BUV737, CD14 and CD127 BUV805 (BD Biosciences), CD86 and TIGIT BV421 (BD Biosciences), IgD, CD27 and ICOS SuperBright436 (Thermo Fisher Scientific, Waltham, MA, USA), CD27, HLA-DR and Helios Pacific Blue, CD40L and TCRvα2 BV480, ICOS-L, CD45RA, CD28, NKp46 BV510, CD33 and CD19 BV570, BDCA-2 and Tim-3 BV605, Lag-3, CD103 and NKp30 BV650, Tim-3, CCR8, CD101 and CD127 BV711, CD3 Alexa532, CD15, CD96, T-bet, 2B4 and BTLA PerCPCy5.5 (BioLegend), PD-L1, CD39, Eomes and 4-1BB PerCPeFluor710 (BioLegend), CD112, CD226, TCF-1, BTLA, CD160 PE (BioLegend), CD155, CTLA-4 and TCRvα7.2 PE-Dazzle594 (BioLegend), HLA-DR, 4-1BB, CD161 and OX40 PE-Cy5 (BD Biosciences), CD68 and TCRγδ1 PE-Cy7 (BioLegend), VISTA, CRTAM, granzyme A, CXCL-13 APC (Thermo Fisher Scientific), CD38 APC/Cy5.5 (Thermo Fisher Scientific), CD11c, granzyme B, NKG2A Alexafluor700 (BD Biosciences), CD112R Alexafluor700 (Biotechne), CD83, CCR7, perforin and CD57 APC/Fire750 (BioLegend). Spectral flow cytometry was carried out on a Cytek Aurora flow cytometer (Cytek Biosciences, Fremont, CA, USA). Supervised analysis was performed with FlowJo (BD Biosciences) for fine adjustments of channel spillovers and live cell subset extraction for unsupervised analysis. Unsupervised analysis was performed using the R Programming Language v3.6.0 with the CATALYST package v1.8.7, using a modified version of a previously published procedure (*20, 21*). Briefly, marker expression was transformed using arcsinh with a cofactor of 150. Samples were z-scored per batch to remove batch effects. Events that were more than five standard deviations away from the mean were removed. Events from all samples were clustered per panel and manually labeled based upon their mean fluorescence intensity (MFI) of lineage and differentiation markers. Clusters with the same label were combined. Visualization was performed using Uniform Manifold Approximation and Projection (UMAP) reduction. The frequency of cells for each sample was calculated by dividing the number of cells in a cluster by the total number of cells for that sample. To evaluate differences in cell frequency, unpaired *t*-tests were performed between the abundance of Rs and NRs for each cell type. For each cluster, unpaired *t*-tests were performed between the median expression of Rs and NRs.

Antibodies Used for Multiparameter Spectral Flow Cytometry

Fluorochrome	Panel 1	Panel 2	Panel 3	Panel 4	Panel 5
BUV395	CD1a	CXCR-5	CXCR-5	CXCR-5	CXCR-5
BUV496	CD16	CD16	CD16	CD16	CD16
BUV563	CD123	CD25	CD25	CD25	CD25
BUV661	CD56	CD56	CD56	CD56	CD56
BUV737	CD19	CD8	CD8	CD8	CD8
BUV805	CD14	CD127	CD127	CD14	CD14
BV421	CD86	TIGIT	TIGIT	TIGIT	TIGIT
Super Bright 436	IgD	CD27	ICOS	CD27	ICOS
Pacific blue	CD27	HLA-DR	Helios	HLA-DR	CD27
BV480	CD40	TCRgd2	TCRgd2	TCRgd2	TCRgd2
BV510	ICOS-L	CD45RA	CD28	NKp46	CD28
BV570	CD33	CD19	CD19	CD19	CD19
BV605	BDCA-2	TIM-3	TIM-3	TIM-3	TIM-3
BV650	Lag-3	Lag-3	CD103	NKp30	CD103
BV711	TIM-3	CCR8	CD101	CD127	CD127
BV750	CD11b	CD4	CD4	CD4	CD4
BV785	CD141	PD-1	PD-1	PD-1	PD-1
FITC	CD80	Ki67	Ki67	Ki67	Ki67
Alexa flor 532	CD3	CD3	CD3	CD3	CD3
PercP-Cy 5.5	CD15	CD96	T-bet	2B4	CD160
PercP-EFluor710	PD-L1	CD39	Eomes	PD-L1	TCR aV7.2
PE	CD112	CD226	TCF-1	BTLA	CD161
PE-Dazzle 594	PVR	CTLA-4	TCRva7	Blimp-1	BTLA
PE-Cy5	HLA-DR	4-1BB	CD161	OX40	4-1BB
PE-Cy7	CD68	TCRgd1	TCRgd1	TCRgd1	TCRgd1
APC	VISTA	CRTAM	GRZ-A	CXCL-13	Granzyme A
APC-Cy5.5	CD38	CD38	CD38	CD38	CD38
AlexaFluor700	CD11c	PVRIG	GRZB	NKG2A	Granzyme B
Zombie NIR	Viability	Viability	Viability	Viability	Viability
APC-Fire750	CD83	CCR7	Perforin	CD57	Perforin

Single-cell RNA Sequencing of Tumor Samples

Fluorescence-activated cell sorting-isolated $CD45^+$ cells from tumor biopsies were processed using 10X Genomics' Chromium platform for droplet-based single-cell RNA sequencing (scRNA-seq). Eleven samples were collected at day 0, nine samples were collected around day 56, and one sample was collected at day 129. Gene expression libraries were generated using the Chromium Single Cell 5' Library Construction Kit (v1.0 chemistry, PN-1000006) following the CG000086 user guide. Each library was sequenced on the Illumina

NovaSeq 6000 System with a PE150 configuration to a target depth of 50 k read pairs per cell. Sequenced gene expression libraries were aligned to the GRCh38-2020-A reference genome using 10X Genomics' Cell Ranger count v4.0.0 with default settings. Cell count matrices were loaded into R and processed using the standard workflow of Seurat v3.2.0 (*29*). Feature counts were normalized using NormalizeData with default settings. This function divides the feature counts of each cell by the total counts for that cell, multiplied by 10,000, followed by taking the natural log. Then T and B cell V, D, J, and C genes were removed to prevent clustering by clonotype. Any gene with the following prefixes were removed: TRA(VDJC)-, TRB(VDJC)-, TRD(VDJC)-, TRG(VDJC)-, IGH(VDJC)-, IGL(VDJC)-, IGK(VDJC)-. Cells were removed in which the percentage of reads that aligned to the mitochondrial genome was greater than 10%. To exclude empty droplets and multiplets, cells with unique feature counts less than 200 or greater than 3000 were excluded. Any sample that had fewer than 300 cells after the previous quality control step was removed. Variable gene features were identified using FindVariableFeatures with default settings. Batch effects were removed using FindIntegrationAnchors and IntegrateData with default settings. Integrated expression data were scaled and centered using ScaleData with default settings. Clustering was performed using FindNeighbors and FindClusters using default settings. Each cluster was identified based upon gene expression. To facilitate this process, differential gene expression between each cluster and all other clusters was performed using FindMarkers with a min.pct=0.25. Two clusters that were identified as melanoma contamination (SPP1high, APODhigh) and one cluster that was likely dead or dying cells were removed. Clusters identified as the same cell type were merged. The top 50 genes for each cell type after this process are shown in **Table S4**. At this point, samples that contained fewer than 300 cells were removed because of potential bias they could introduce in abundance calculations. A UMAP projection was calculated using RunPCA and RunUMAP. Abundance for each sample was calculated by dividing the number of cells of a particular cell type by the total number of cells for that sample. Unpaired *t*-tests between Rs and NRs were performed for each cell type before and after (day 56) treatment. Uncorrected p-values were reported due to the low number of samples. Phenotype differences between Rs and NRs were calculated by only selecting cells from samples collected post-treatment (day 56) and running FindMarkers on each cell type between cells from Rs and NRs.

Cytokine/Chemokine Multiplex Analysis

Serum samples were analyzed by Eve Technologies (Calgary, Canada) using the Human Cytokine Array/Chemokine Array 65-Plex Panel (HD65) [EGF, Eotaxin, FGF-2, Flt-3 Ligand, Fractalkine, G-CSF, GM-CSF, GRO, IFN-α2, IFN-γ, IL-10, IL-12 (p40), IL-12 (p70), IL-13, IL-15, IL-17A, IL-18, IL-1RA, IL-1α, IL-1β, IL-2, IL-3, IL-4, IL-5, IL-6, IL-7, IL-8, IL-9, IP-10, MCP-1, MCP-3, MDC (CCL22), MIP-1α, MIP-1β, PDGF-AA, PDGF-AB/BB, RANTES, TGFα, TNF, LTα, VEGF-A, sCD40L, Eotaxin-2, MCP-2, BCA-1, MCP-4, I-309, IL-16, TARC, 6CKine, Eotaxin-3, LIF, TPO, SCF, TSLP, IL-33, IL-20, IL-21, IL-23, TRAIL, CTACK, SDF-1, ENA-78, MIP-1d, IL-28A]. Data obtained were log2-transformed and quantile-normalized, and statistical tests were performed [principal component analysis (PCA), analysis of variance (ANOVA), *t*-test]. Data were analyzed and visualized using Partek Genomic suite 6.0 (Partek Inc., St. Louis, MO, USA).

Metabolome and Lipidome Analysis

Samples were analyzed by Metabolon, Inc. (Durham, NC, USA). Serum samples were analyzed using liquid chromatography-tandem mass spectrometry and gas chromatography-mass spectrometry. Peaks were identified using Metabolon's proprietary chemical reference library. Resultant chemicals were mapped to known classes of biological molecules and metabolic pathways using the Kyoto Encyclopedia of Genes and Genomes database. Both lipidomic and metabolomic datasets were log2-transformed and quantile-normalized, and statistical tests were performed (PCA, ANOVA, *t*-test). Data were analyzed and visualized using Partek Genomic suite 6.0 (Partek Inc.).

Statistical Analyses

Time to progression for recipients was defined as the interval (in months) from day 0 (FMT administration) to the date of radiographic progression. Patients who did not progress were censored at their date of last contact. Overall survival for recipients was defined as the interval (in months) from day 0 (FMT administration) to the date of death. Patients who were alive as of September 1, 2020 were censored at their date of last contact. Time to progression for FMT donors was defined as the interval (in months) from date of PD-1 therapy initiation to date of last contact.

Transkingdom Network Analysis of Multiomic Data

Network Reconstruction: To create a statistical model of robust interactions between the different players, we created a transkingdom network independent of a particular group or patient (*41*). First, we identified elements (serum cytokines, serum metabolites, multi-parameter flow cytometry, and stool bacteria) that differentially changed upon FMT treatment in Rs compared with NRs. Next, Spearman rank correlation was calculated between all pairs of elements. To keep robust relationships, interactions not involving bacteria were selected if they had the same sign of correlation in: (i) NRs pre-FMT, (ii) Rs pre-FMT, (iii) NRs post-FMT, and (iv) Rs post-FMT. For within- and inter- omic interactions involving bacteria, only the post-FMT groups (iii and iv) were used to check for consistent signs of correlation. Additionally, pairs were included in the network if they satisfied principles of causality (i.e., satisfied fold-change relationship between the two partners in Rs vs. NRs post-FMT) (*42*) and 5% combined p-value cutoff for meta-analysis of correlations based on Fisher's z transformation of correlations (metacor in R package meta v4.9-7). Finally, 1% false discovery rate (FDR) was used for edges involving bacteria or within edges (except flow), whereas 2.5% FDR was used for edges involving flow cytometry parameters or inter-omic edges, and edges involving metabolites also had 30% individual (within group) p-value cutoff.

Detecting Gene Expression Subnetworks: Cytoscape Software 2.6.3 was used to visualize the networks (*43*). To identify subnetworks in the transkingdom network, we used the MCODE v1.2 (Molecular Complex Detection) (*51*) plug-in for Cytoscape to identify clusters (subnetworks). The largest subnetwork containing nodes from all four different omics data was selected for further investigation.

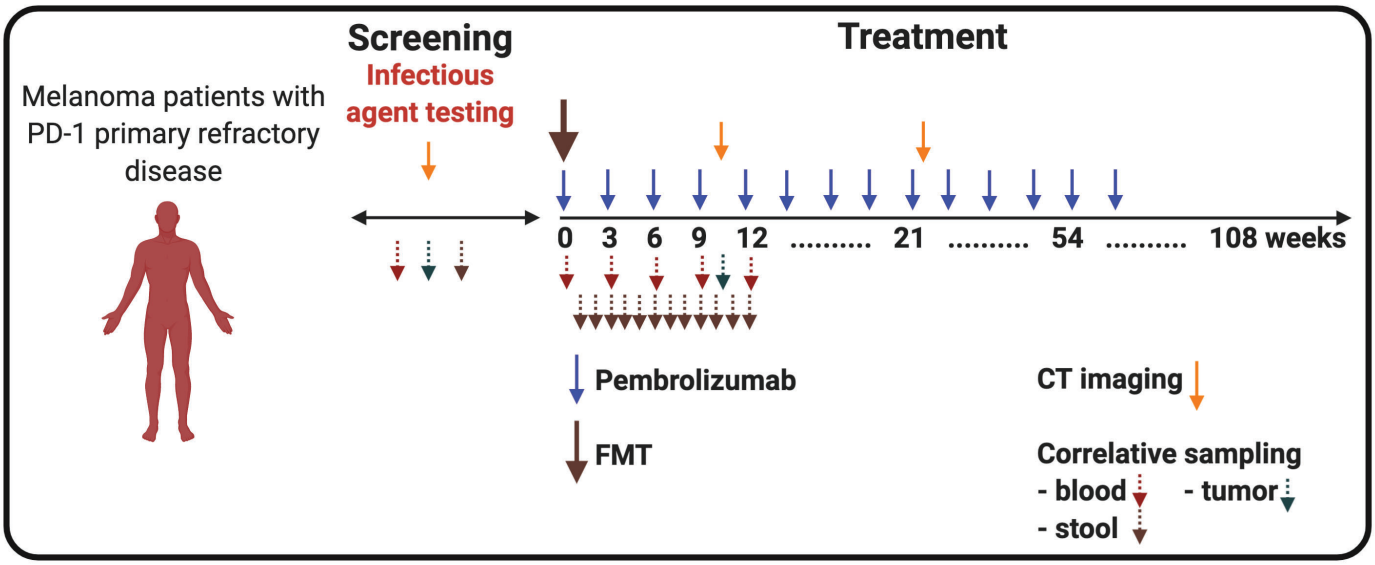

Figure S1.
Clinical Trial Schema of a Phase II Study of Anti-PD-1 Responder-Derived FMT and Pembrolizumab in PD-1-Refractory Melanoma. Eligible subjects were melanoma patients primary refractory to anti-PD-1 therapy. Patients had received ≥2 cycles of anti-PD(L)1 therapy over ≥6 weeks with best response of PD or SD for <6 months as assessed by RECIST v1.1. Disease progression was confirmed on at least one imaging study before enrollment by an independent radiologist. Other eligibility criteria were no CNS disease, biopsy-amenable disease, and stable organ function. Following screening, which included extensive serological testing (stool, blood) for potentially transmissible infectious agents, and tumor biopsy, patients received a FMT derived from individual melanoma patients with long lasting objective response to anti-PD1 therapy. FMT administered colonoscopically on day 0 along with pembrolizumab (200 mg). Pembrolizumab was repeated every 3 weeks. Tumors were rebiopsied at weeks 9–12, and blood and stool were resampled periodically. Restaging scans were performed at weeks 9–12 and repeated every 9–12 weeks while on study. Patients remained on study until intolerable toxicity, RECIST v1.1 confirmed disease progression, or completion of 35 cycles of pembrolizumab.

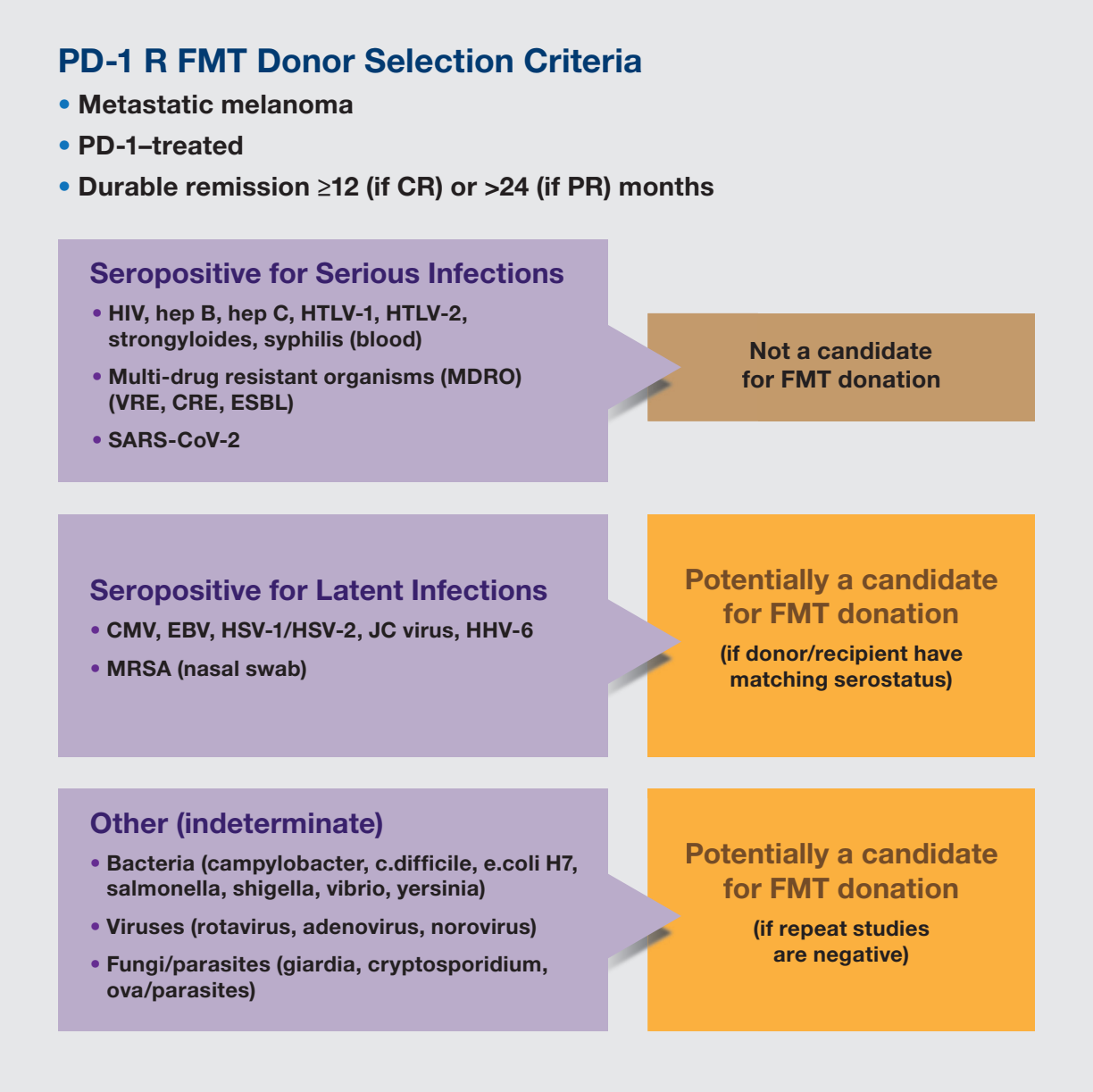

Figure S2.
Testing Methodology Used to Evaluate Recipient and Donor Suitability.

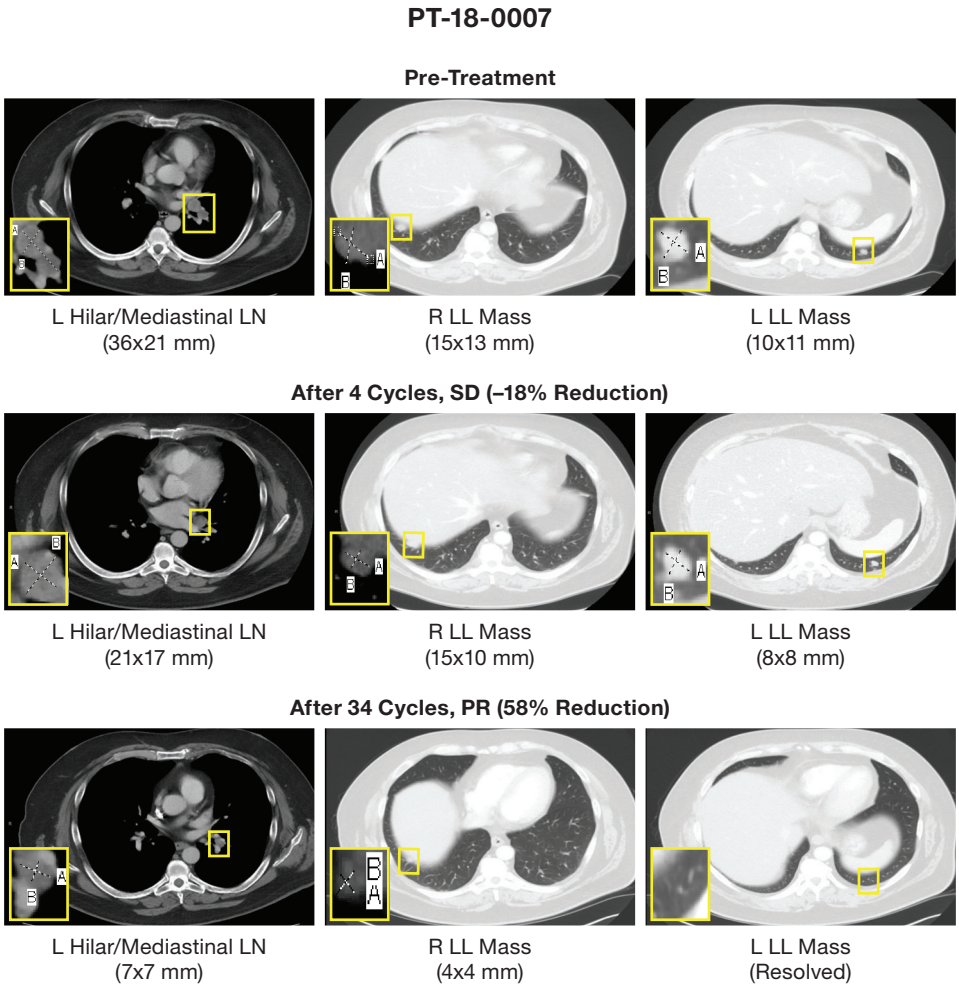

Figure S3.
Representative CT Scan Images From Patient PT-18-0007 Treated on Phase II Study of Anti-PD-1 Responder-Derived FMT and Pembrolizumab in PD-1-Refractory Melanoma.

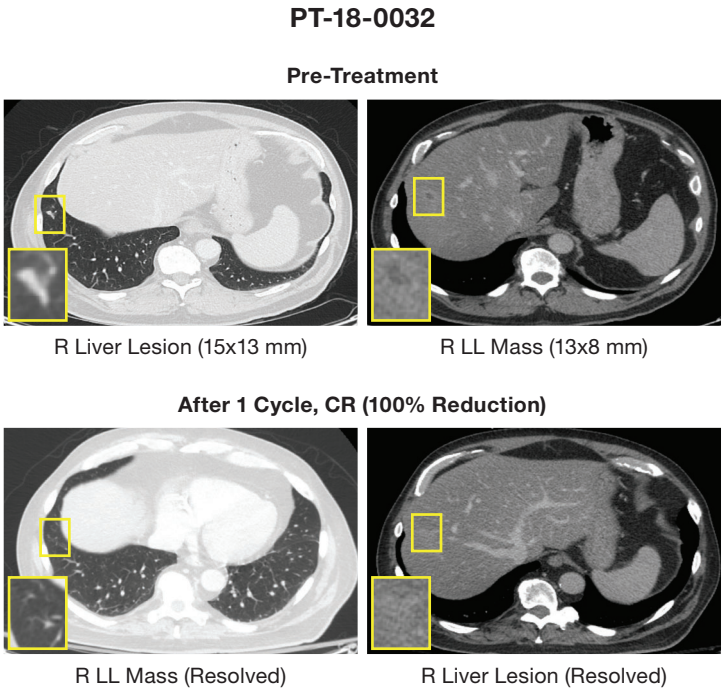

Figure S4.
Representative CT Scan Images From Patient PT-18-0032 Treated on Phase II Study of Anti-PD-1 Responder-Derived FMT and Pembrolizumab in PD-1-Refractory Melanoma.

A

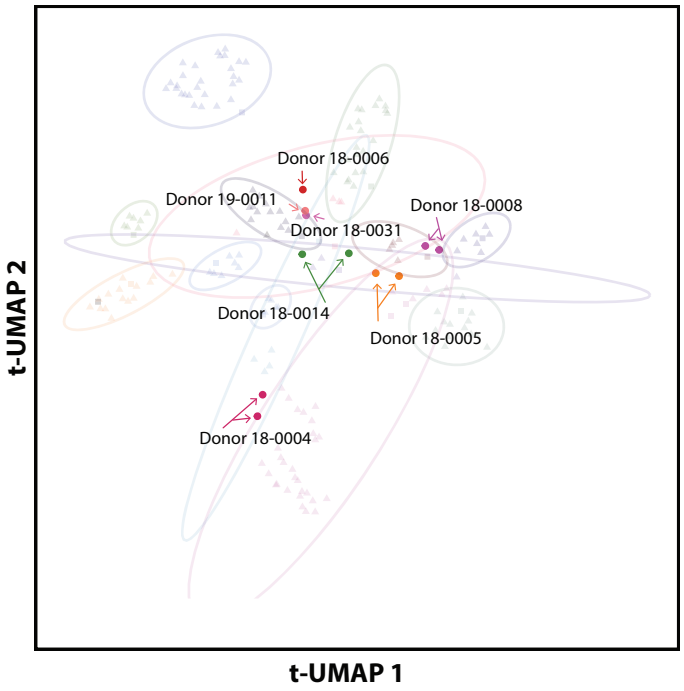

B

FMT Donor ID	FMT Donor Radiographic Response Status (RECIST v1.1)	R	NR	Total
PT-18-0002	CR	1	1	2
PT-18-0005	CR	1	1	2
PT-18-0006	CR	1	0	1
PT-18-0008	PR	1	3	4
PT-18-0014	PR	2	2	4
PT-18-0031	PR	0	1	1
PT-19-0011	CR	0	1	1

C

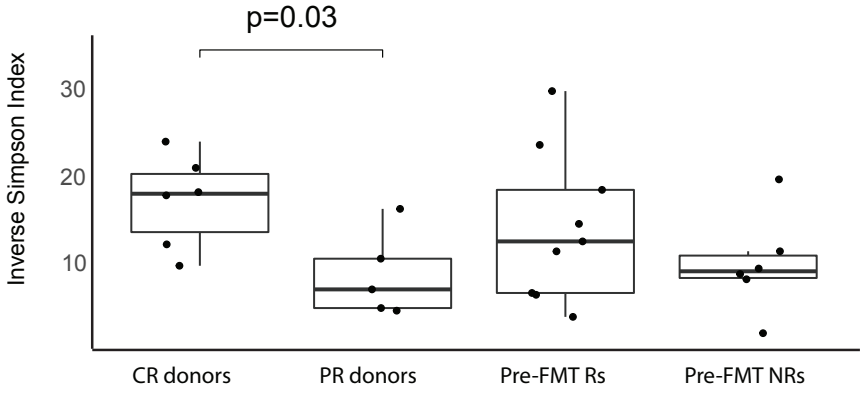

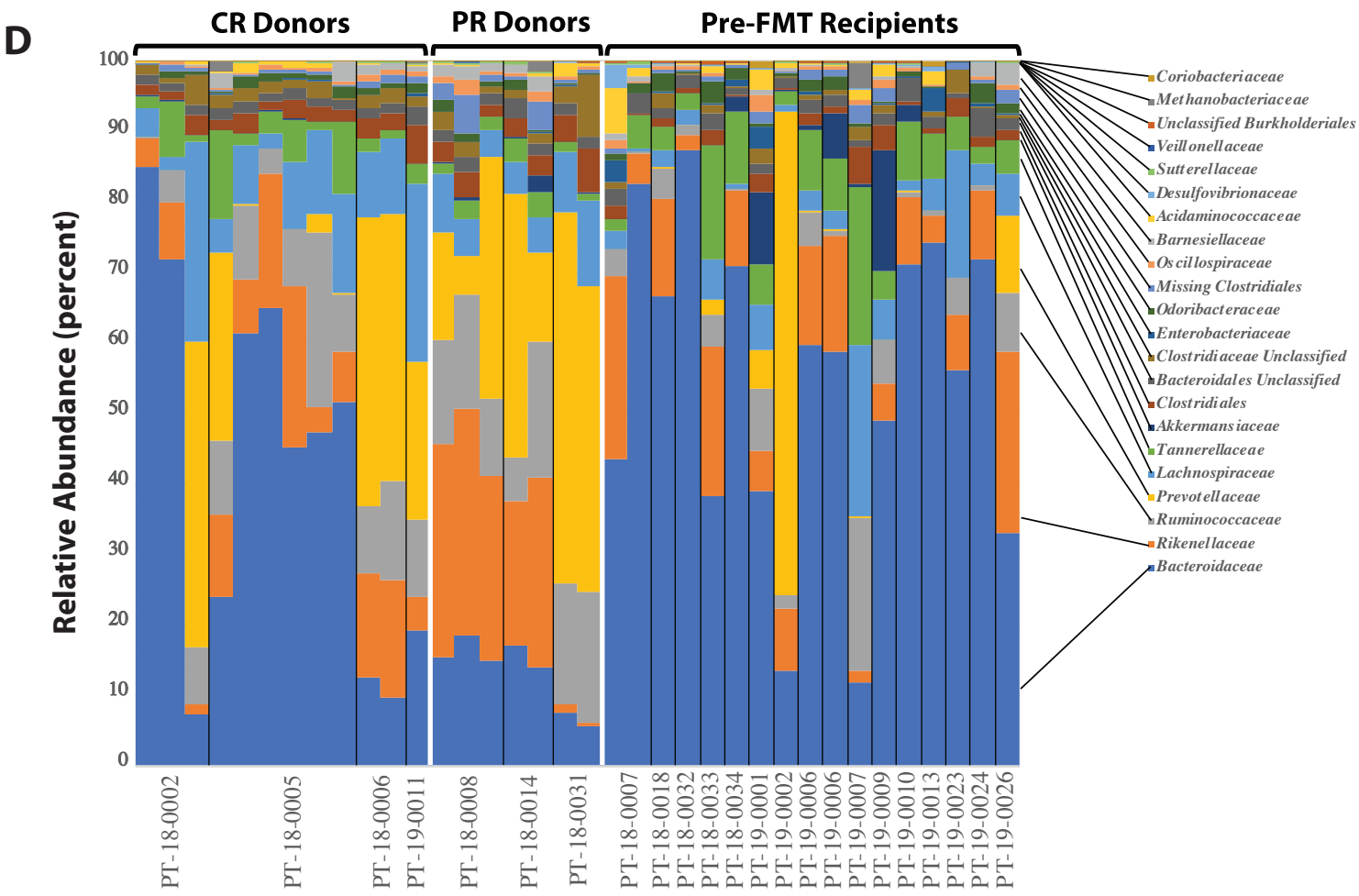

Figure S5.

Metagenomic Analyses of Fecal Microbiota from FMT Donors (n=7) Compared to pre-FMT Recipients.

A) Dimensionality reduction using t-distributed uniform manifold approximation and projection (t-UMAP) plot of microbial taxa abundances by LKT of FMT donors at different time points. Each color corresponds to a different FMT donor.

B) FMT donor recipient combinations. The anti-PD-1 response status of the donors (CR or PR) and the clinical response in the recipients are reported. The status of the FMT donor (CR or PR) did not significantly affect the probability of clinical response in the recipients [χ^2 (n=15) = 0.4167; p=0.52].

C) Alpha-diversity (Inverse Simpson Index) of the fecal microbiota of FMT donors (CR or PR) and recipients before FMT (Rs and NRs).

D) Taxonomic composition distribution histograms at family level for different fecal microbiota samples obtained from the 7 donors and one sample each (n=15) of recipients pre-FMT.

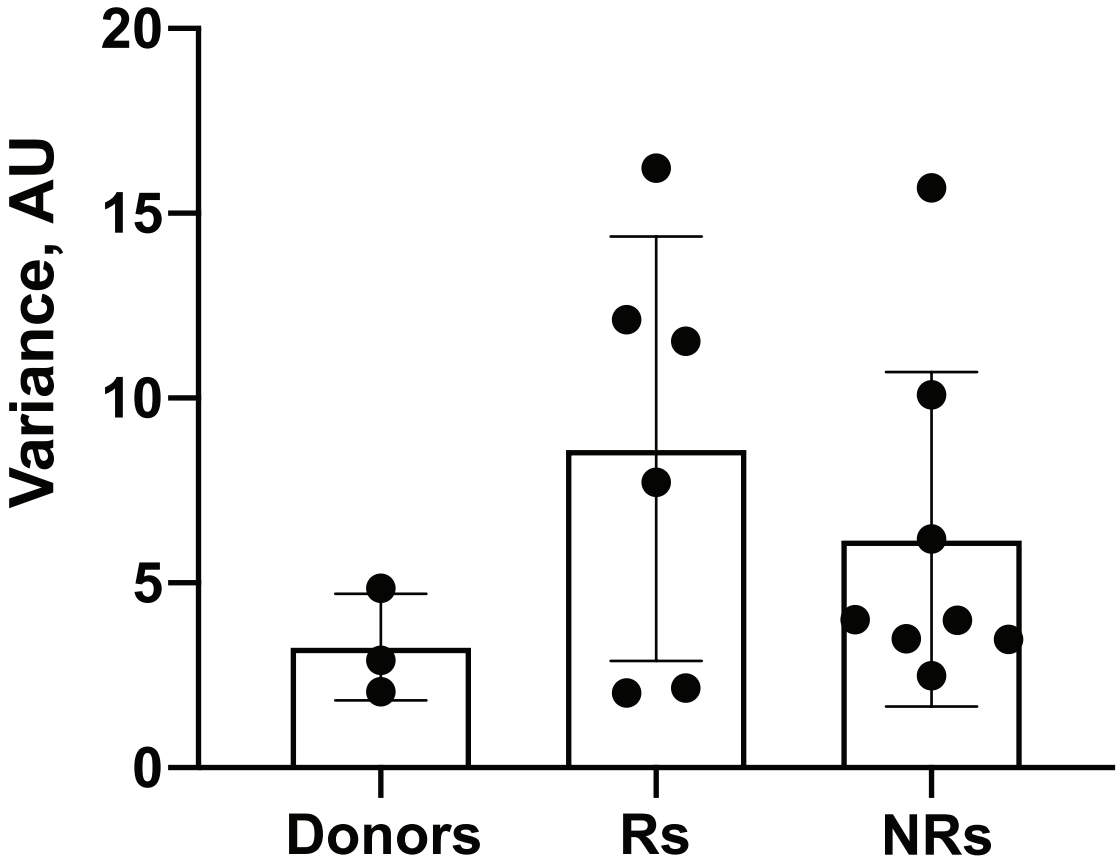

Figure S6:
Intra-Patient Variability of Stool Samples from Donors and Recipients Following Standardization and Dimensionality Reduction. Donors (n=3) and recipients (Rs=6 and NRs=9) who contributed ≥3 fecal samples are depicted. Data were standardized, PCA was performed, PC loading was computed, and variances of patients for every PC loading were calculated as the SD^2/mean and multiplied by the PC variance contribution. Resultant values were added together to produce a combined variance number, which was compared between donors and recipients using the non-parametric t-test.

A. PT–18–0032; FMT Donor PT–18–0014; Complete Response

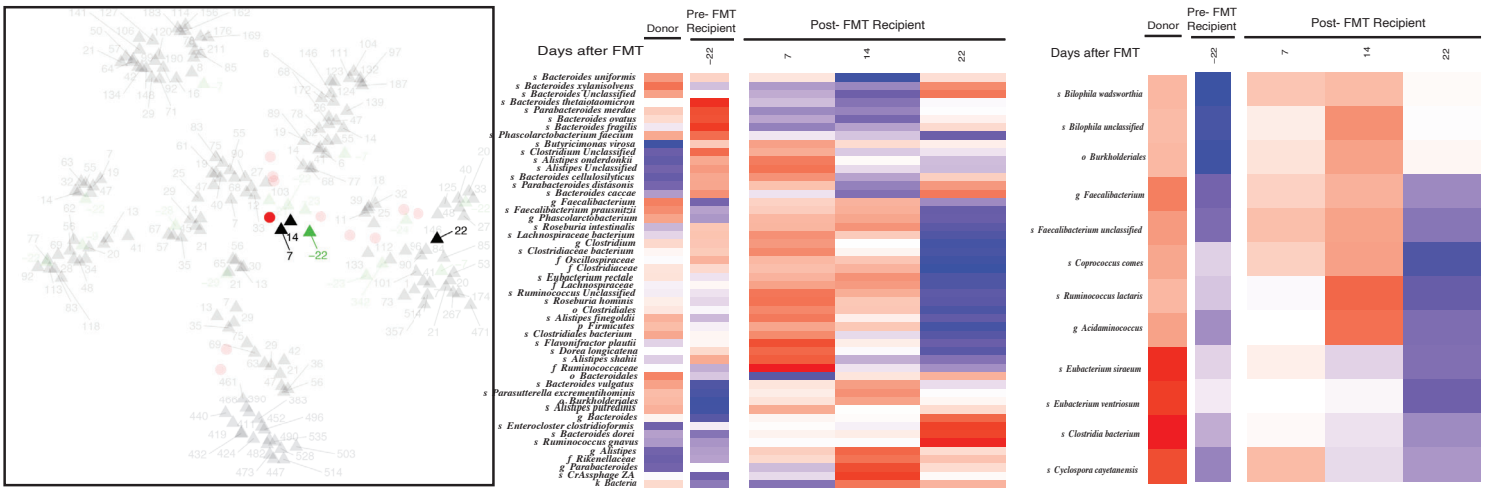

B. PT–18–0007; FMT Donor PT–18–0005 ; Partial Response

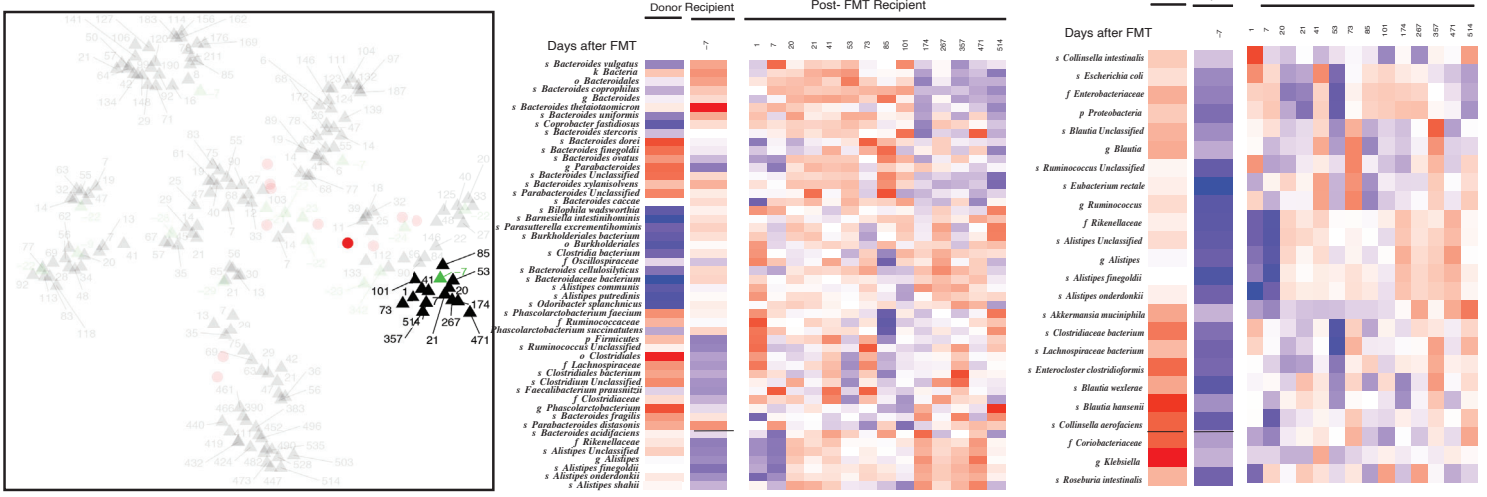

C. PT–19–0024; FMT Donor PT–18–0014; Partial Response

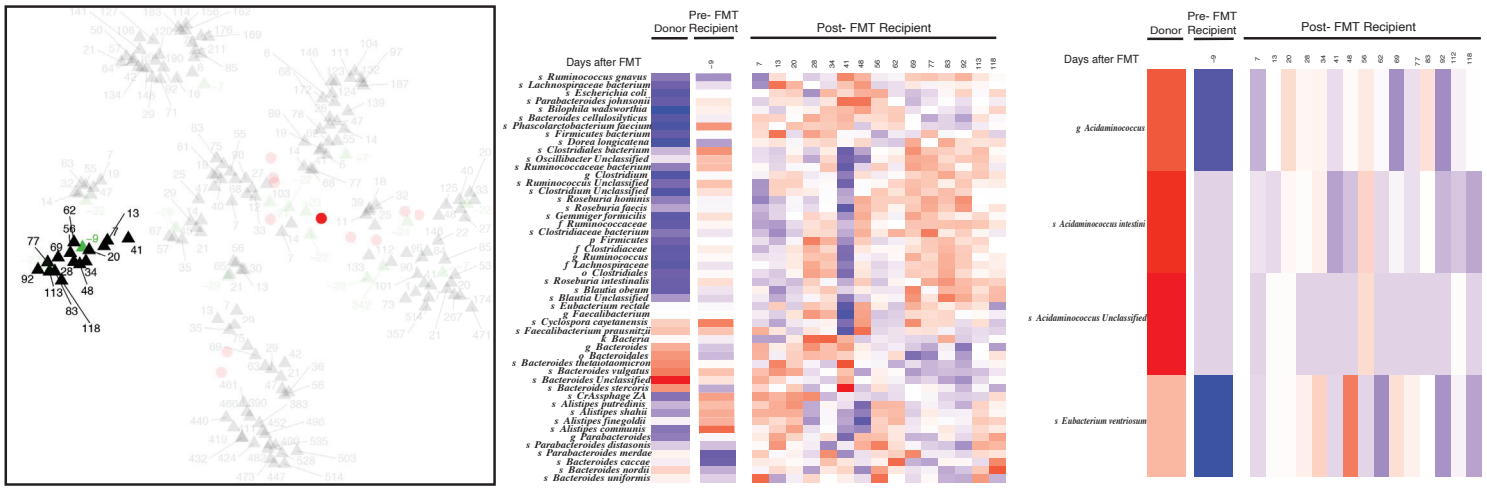

FMT Donor

Recipient Post-FMT

Recipient Pre-FMT

Scaling

Min Max

Davar et al. Figure S7

D. PT–18–0018; FMT Donor PT–18–0002; Stable Disease

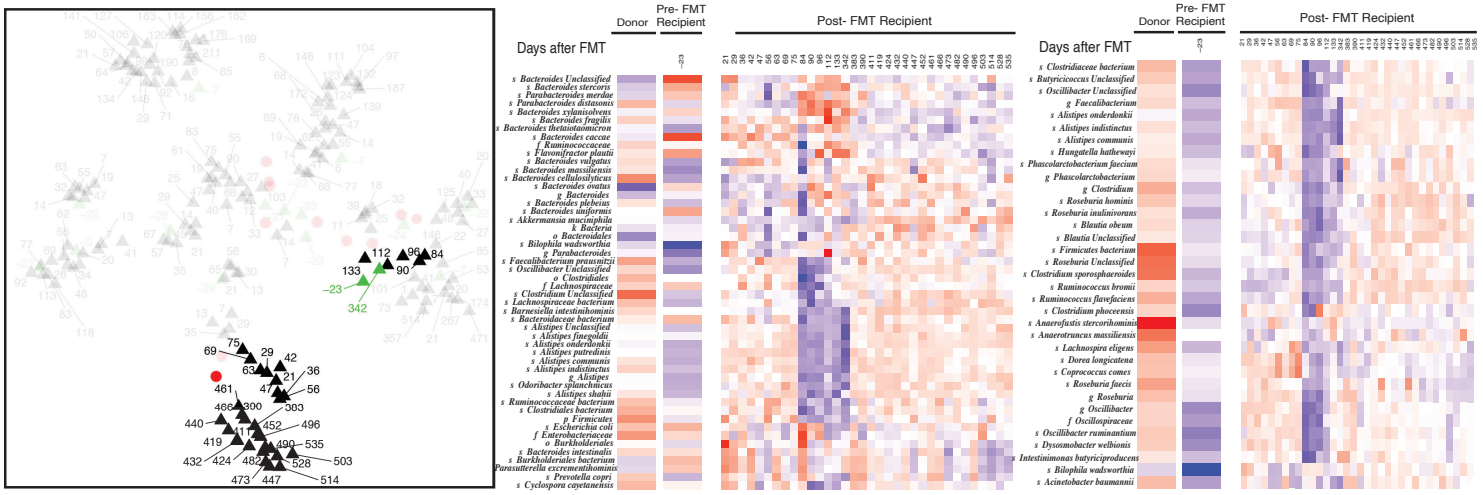

E. PT–19–0002; FMT Donor PT–18–0006; Stable Disease

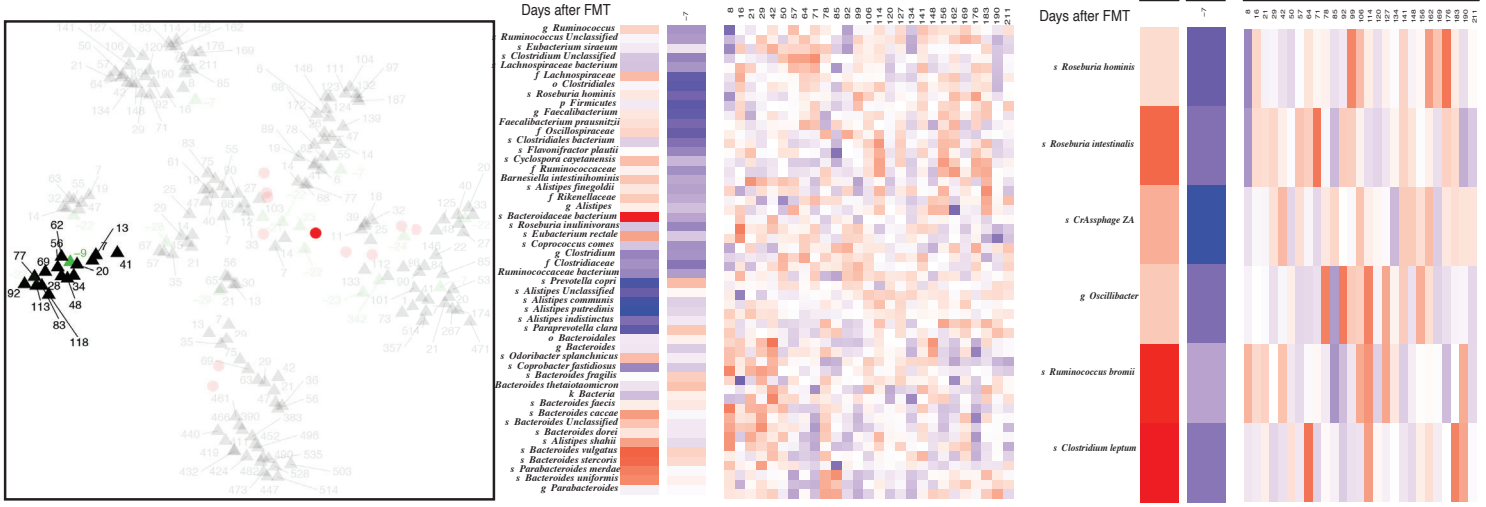

F. PT–19–0010; FMT Donor PT–18–0008; Stable Disease

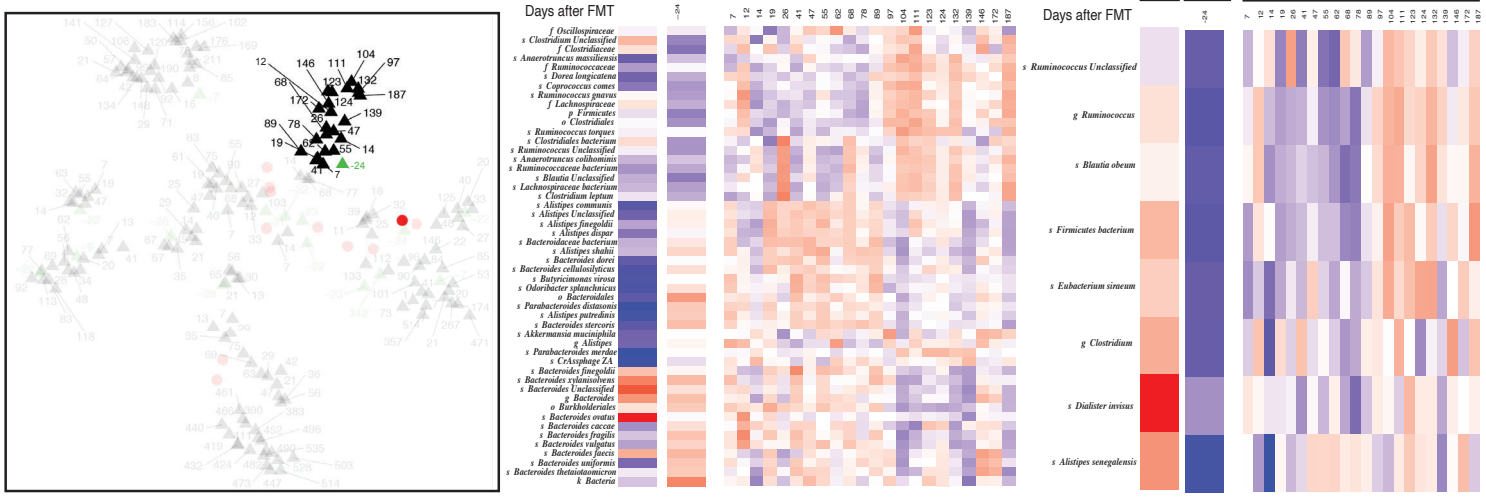

FMT Donor

Recipient Post-FMT

Recipient Pre-FMT

Scaling

Min Max

G. PT–18–0033; FMT Donor PT–18–0008; Progressive Disease

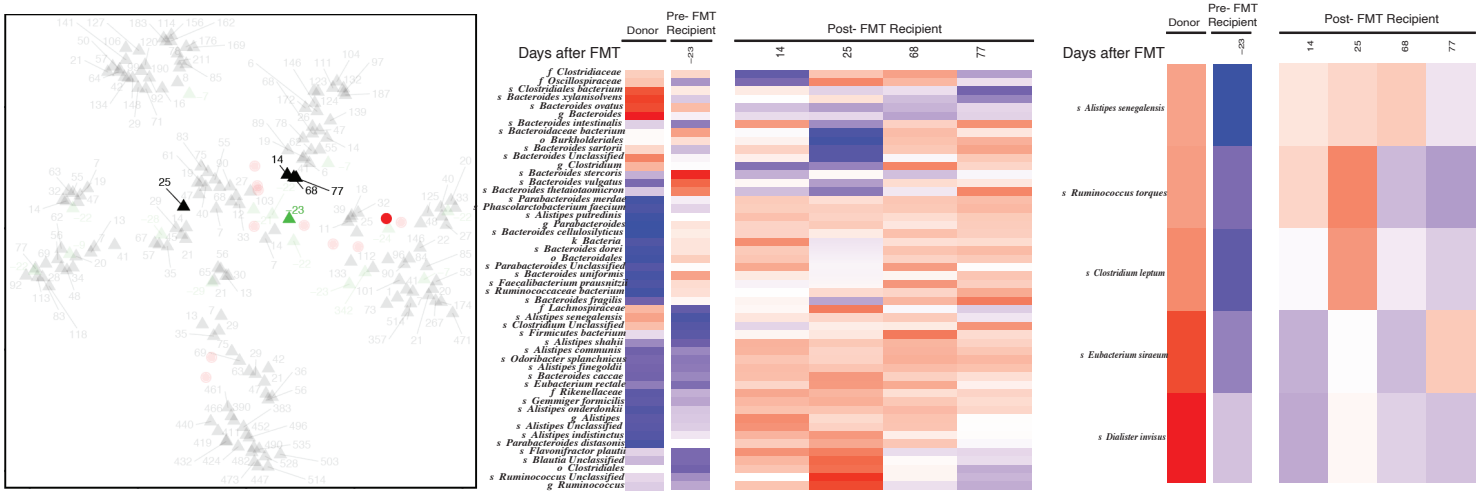

H. PT–18–0034; FMT Donor PT–18–0008; Progressive Disease

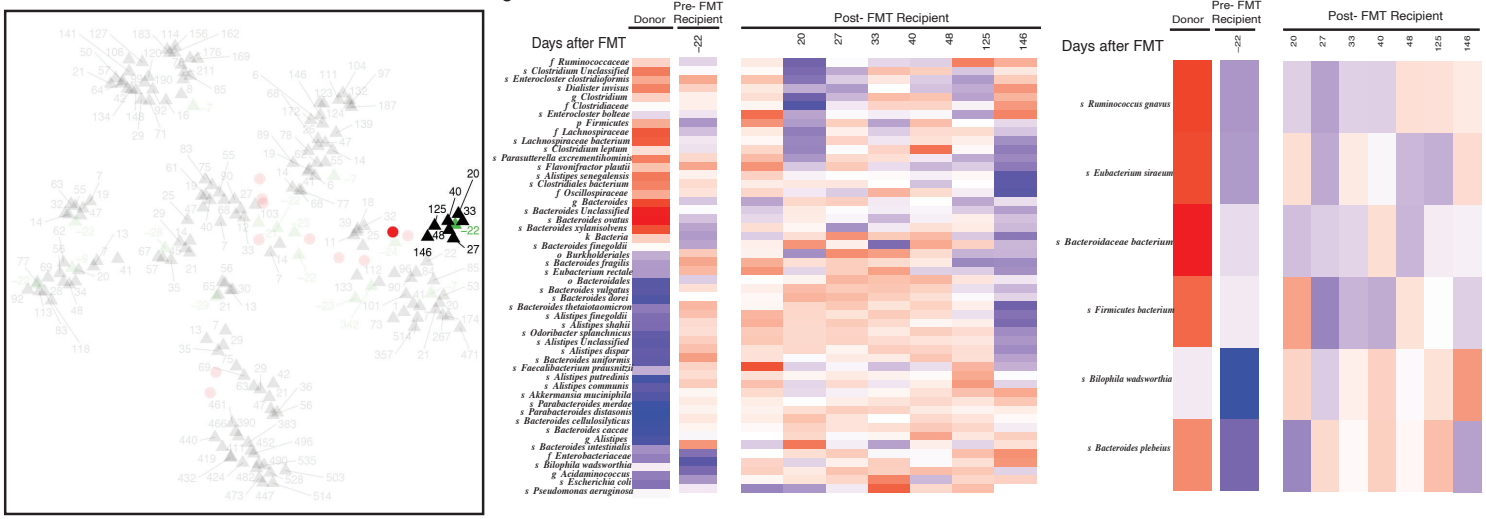

I. PT–19–0007; FMT Donor PT–18–0014; Progressive Disease

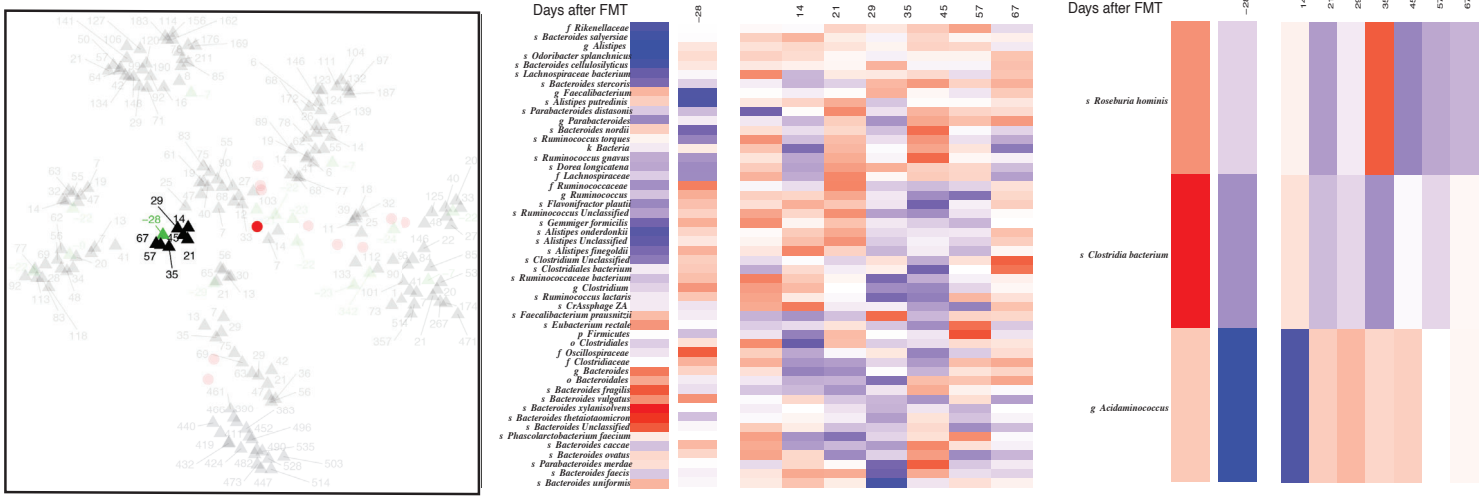

FMT Donor

Recipient Post-FMT

Recipient Pre-FMT

Scaling

Min Max

J. PT–19–0026; FMT Donor PT–18–0014 ; Progressive Disease

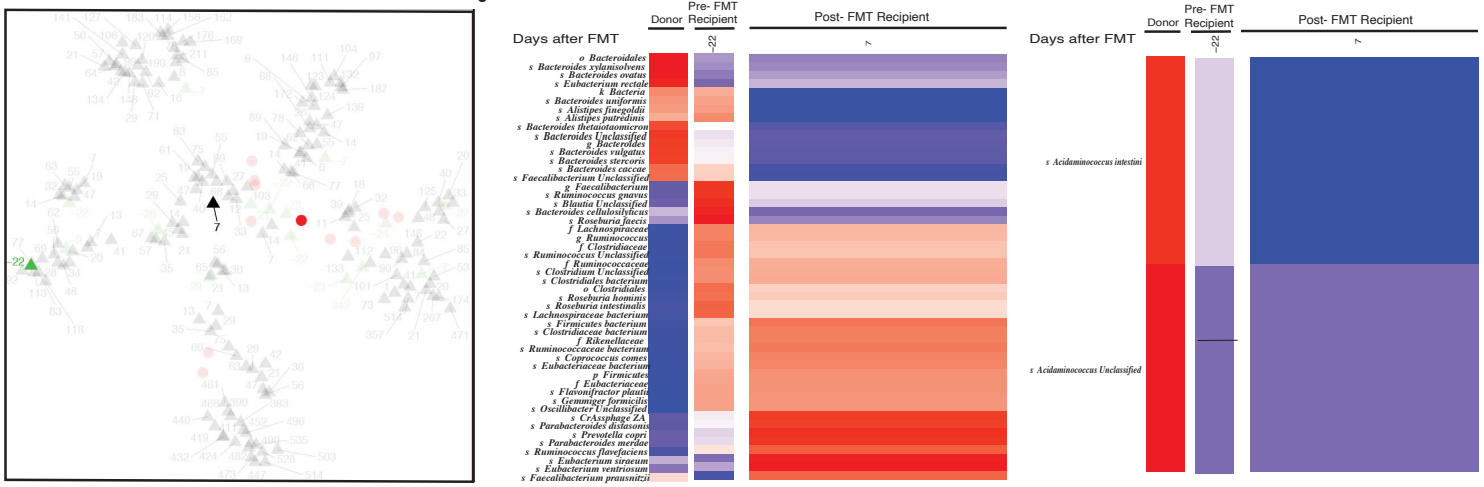

K. PT–19–0013; FMT Donor PT–18–0031; Progressive Disease

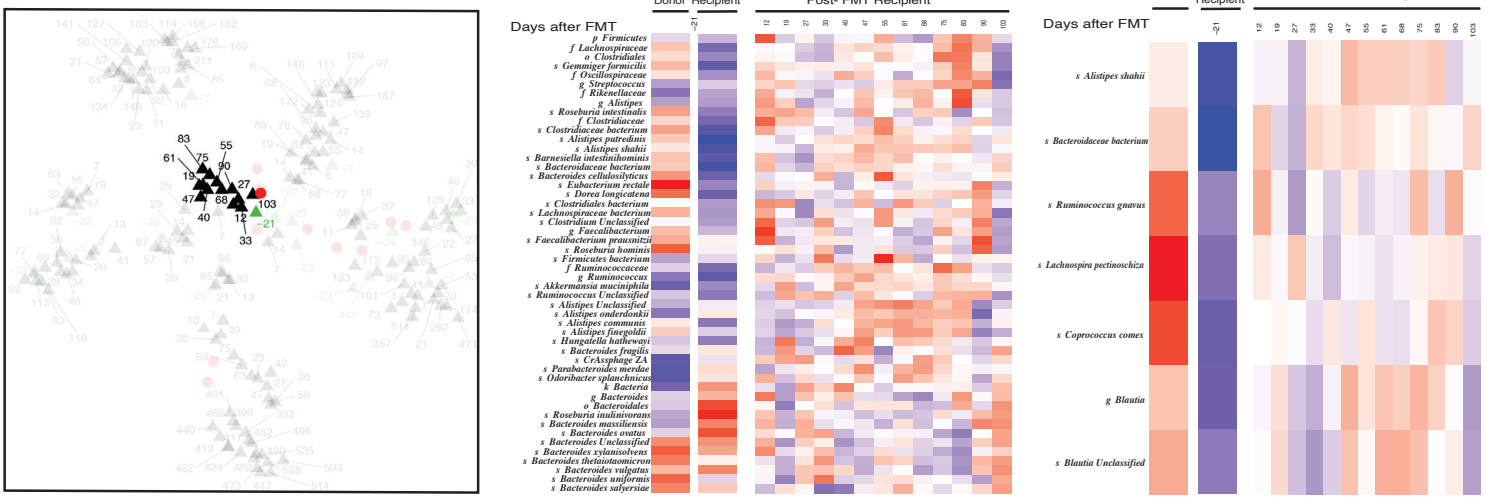

L. PT–19–0023; FMT Donor PT–18–0002; Progressive Disease

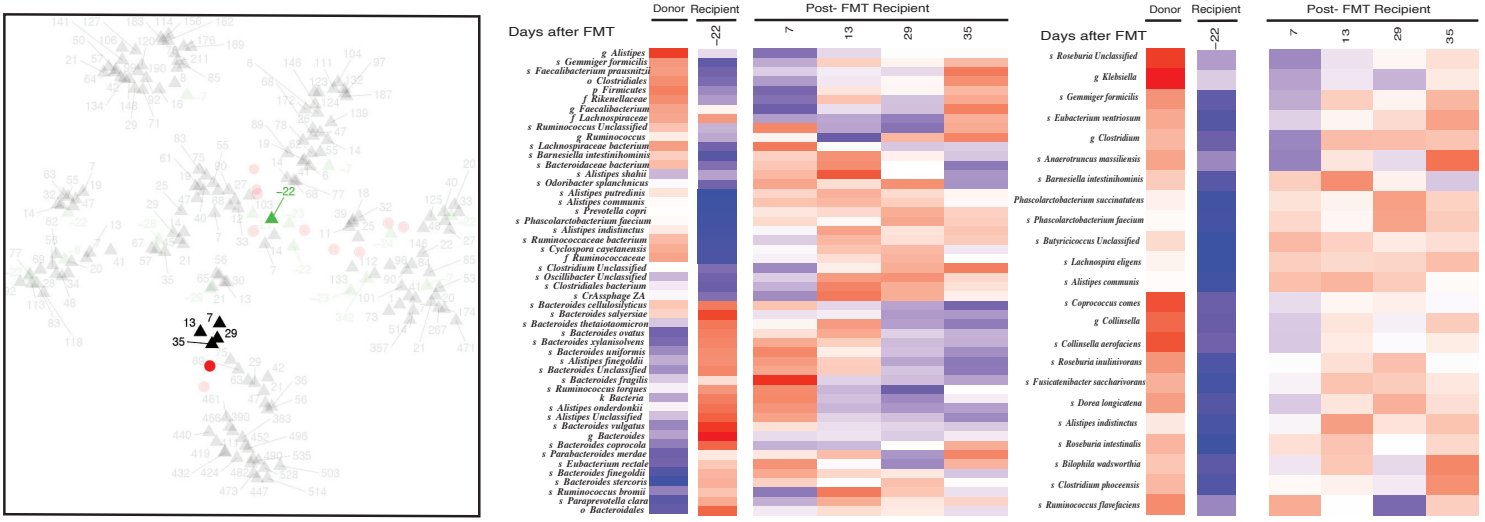

FMT Donor

Recipient Post-FMT

Recipient Pre-FMT

Scaling

Min Max

M. PT–19–0009; FMT Donor PT–18–0008; Progressive Disease

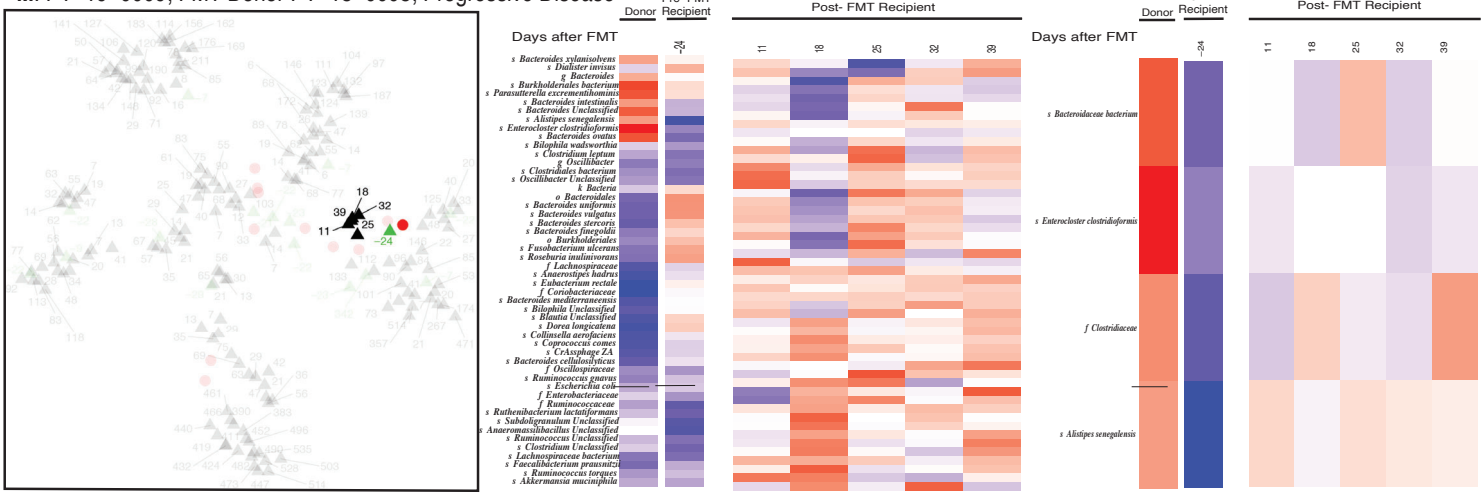

N. PT–19–0006; FMT Donor PT–19–0011; Progressive Disease

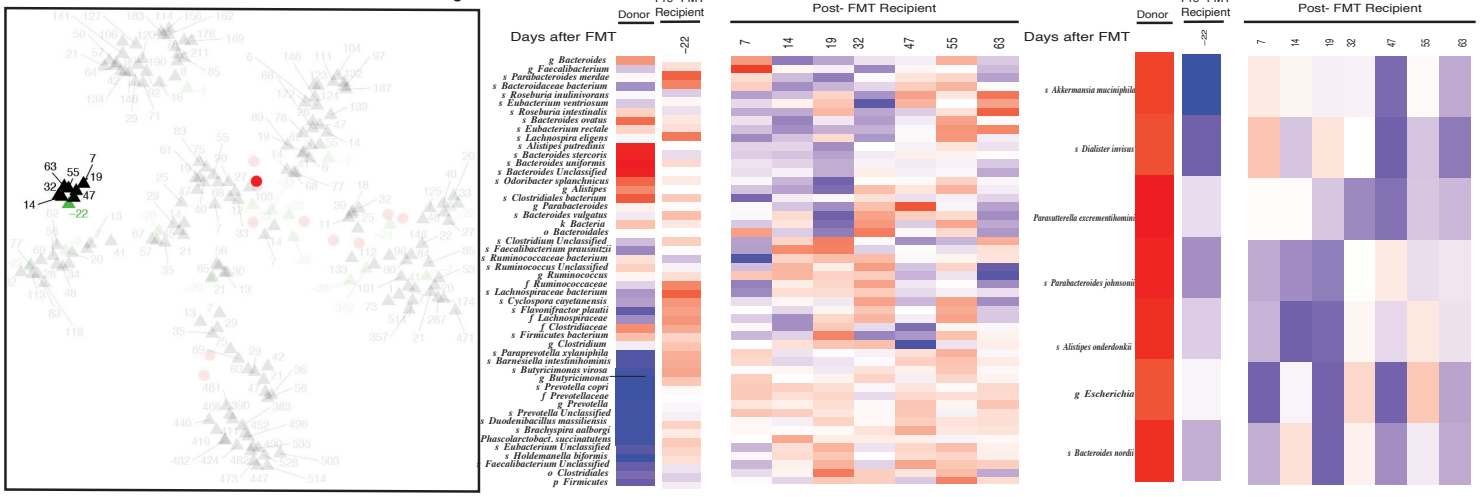

O. PT–19–0001; FMT Donor PT–18–0005; Progressive Disease

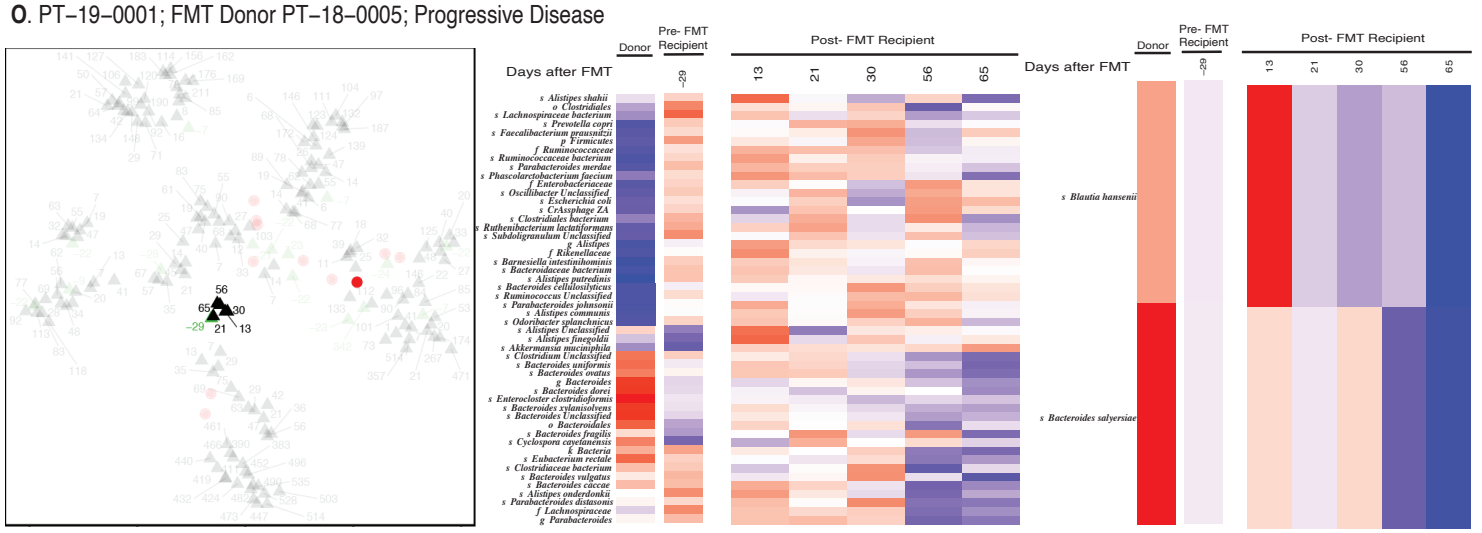

FMT Donor

Recipient Post-FMT

Recipient Pre-FMT

Scaling

Min Max

Figure S7.

Visualization of Metagenomic Data of Gut Microbiome from Patients. Each recipient patient data are depicted in a separate panel (A–O), starting with Rs (PT-18-0032, PT-18-0007, PT-19-0024, PT-18-0018, PT-19-0002, PT-19-0010) and followed by NRs (PT-18-0033, PT-18-0034, PT-19-0001, PT-19-0006, PT-19-0007, PT-19-0009, PT-19-0013, PT-19-0023, PT-19-0026). Results indicate that FMT/pembrolizumab demonstrated substantial colonization by donor microbiota, predominantly in Rs.

For each recipient patient (A-O):

Left: t-UMAP visualization of relative abundances of LKTs of samples involved in all FMT events depicting all samples (light grey triangles), recipient-specific samples (black triangles), pre-treatment sample (green triangle), and donor sample (red circle). Numbers denote the number of days since FMT. Each recipient has only one green triangle, with the exception of PT-18-0018 who received two FMT infusions (two green triangles indicate the two last samples before each FMT treatment).

Center: Relative abundance heatmap of the top 50 most variant LKT across samples. Numbers over each column denote the number of days since FMT. LKTs whose relative abundance was <50 PPM and taxon genome completeness was <5% in at least 5% of samples were discarded.

Right: Engraftment of the LKT present in the donor infusate but not detectable in pre-FMT recipient samples. Relative abundance heatmap of LKTs that were <100 PPM in the pre-FMT recipient sample and >100 PPM in the donor sample. Scaled relative abundances of these LKTs are shown across the samples. Numbers over each column denote the number of days since the FMT.

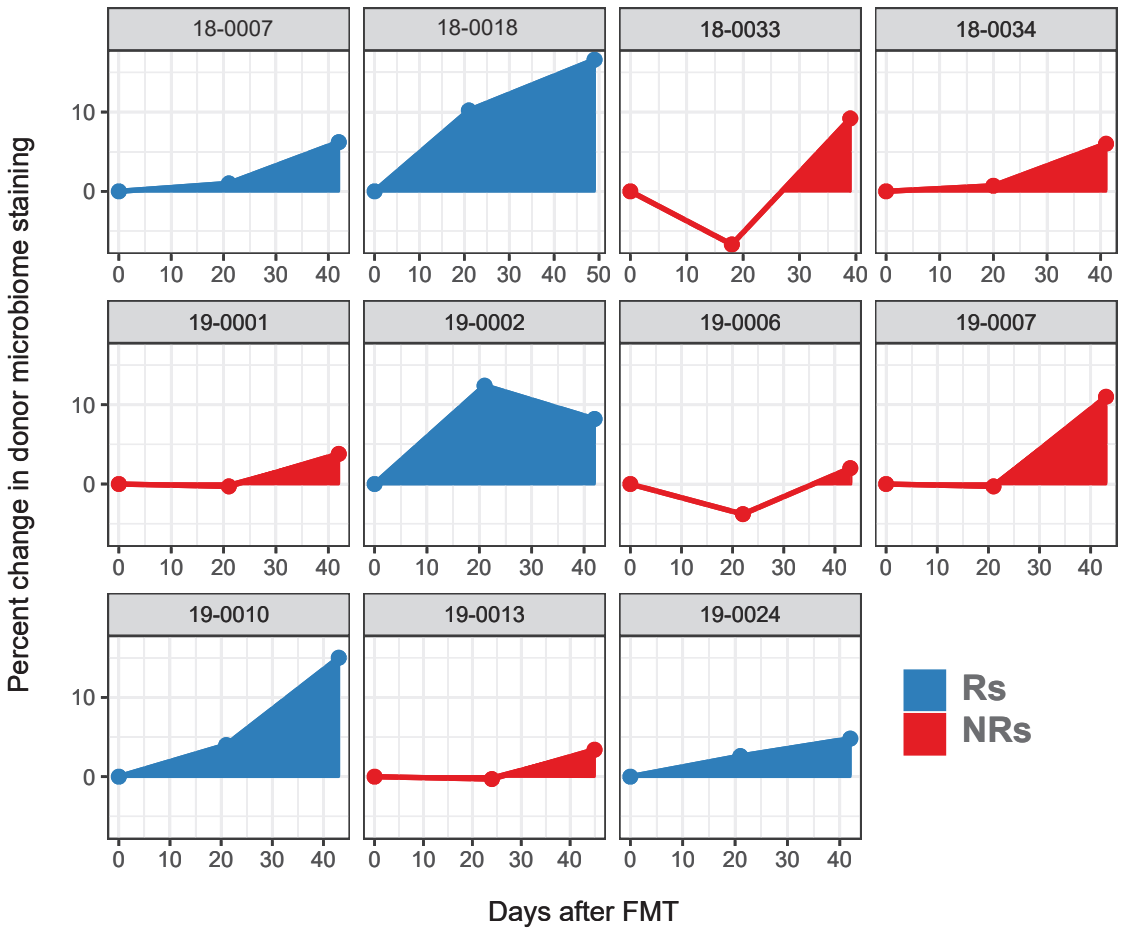

Figure S8.
Recipient Serum IgG Response against Donor Microbiota Following FMT. Donor fecal bacteria were incubated with recipient sera at 1:200 dilutions, washed and stained with PE-labelled anti-human IgG, fixed and analyzed on a flow cytometer. Change in IgG positivity of donor fecal bacteria for each FMT recipient was calculated in relation to the first FMT recipient serum sample available compared to the subsequent two time points up to 50 days later. The shaded area in each box indicates area under the curve (AUC).

Davar et al. Figure S9

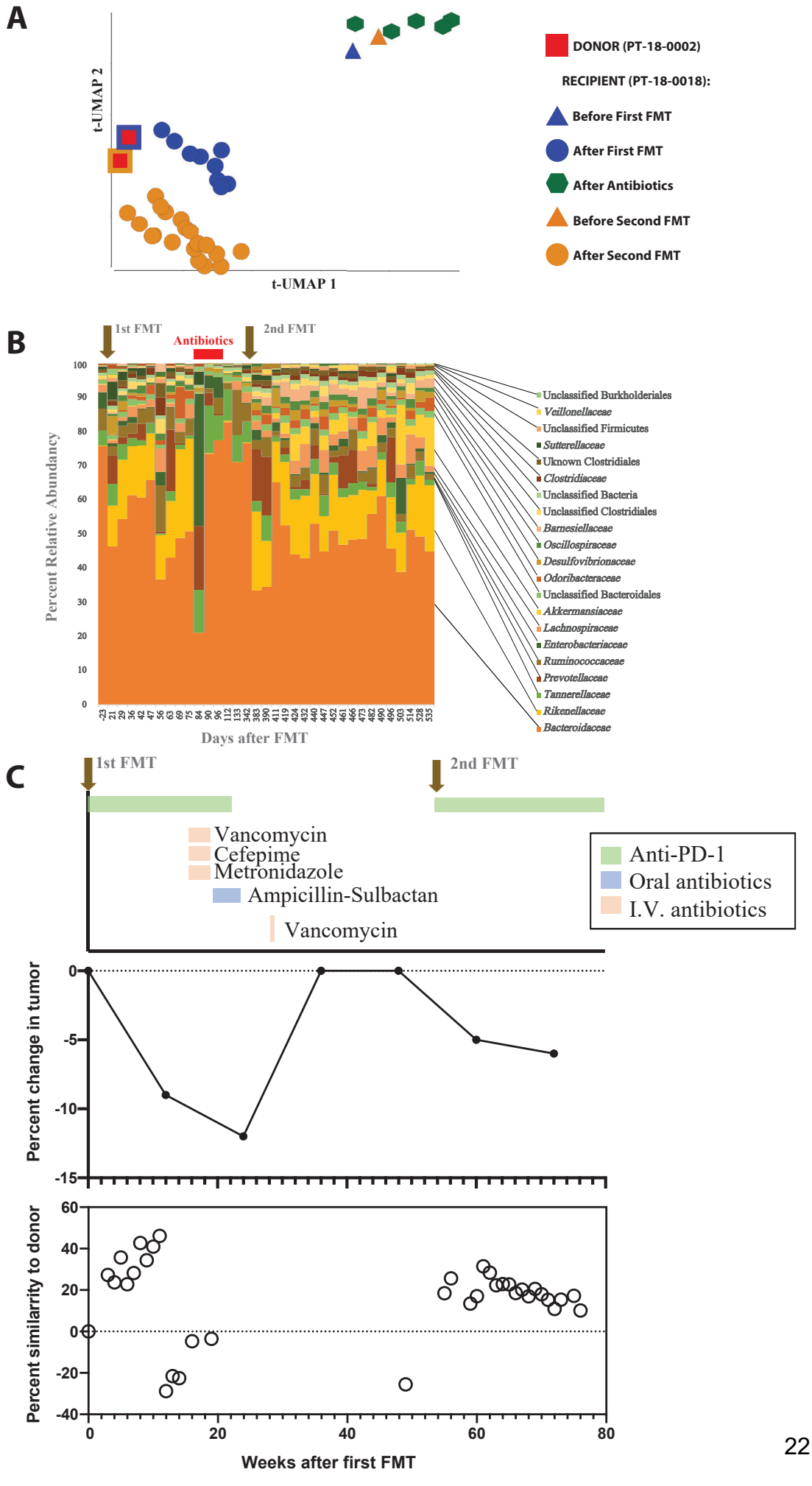

Figure S9.

Visualization of Metagenomic Data of Gut Microbiome from Patient PT-18-0018. Patient PT-18-0018 eleven weeks after FMT developed a soft tissue infection requiring intravenous and subsequent oral antibiotics. A second transplant from the same donor was performed nearly 1 year after initial FMT. A) t-UMAP visualization of fecal microbiota composition of sequential samples from patient PT-18-0018 and, depicted with a red square, the two infusates from donor PT-18-0002 used for the first (blue border) and second (yellow border) FMT. B) Taxonomic composition distribution histograms at family level for the sequential fecal microbiota samples obtained from patient PT-18-0018. C) Treatment schedule, tumor growth and Euclidean distance over time from patients' gut microbiota to the corresponding FMT donor's microbiota. Positive percentage indicates similarity to the corresponding donor while negative percentage indicates changes in the recipient microbiota even further from the donor microbiota.

Davar et al. Figure S10

Figure S10.
Heatmap of Differentially Abundant Taxa Between Pre- and Post-FMT/Pembrolizumab Samples from Rs. Changes of microbiome in Rs and NRs patients were individually evaluated and summary statistics for all samples was calculated using Fisher's method for meta-analyses to estimate statistical significance. Taxa with $p < 0.05$ is shown, Both, p-values and Bonferroni-adjusted p-values are shown next to the taxa. The heatmaps show differentially abundant taxa that were first sorted based on sign of its change (positive or negative) and then ranked by significance and ratio values, with highest significant taxa being on top of its corresponding list.

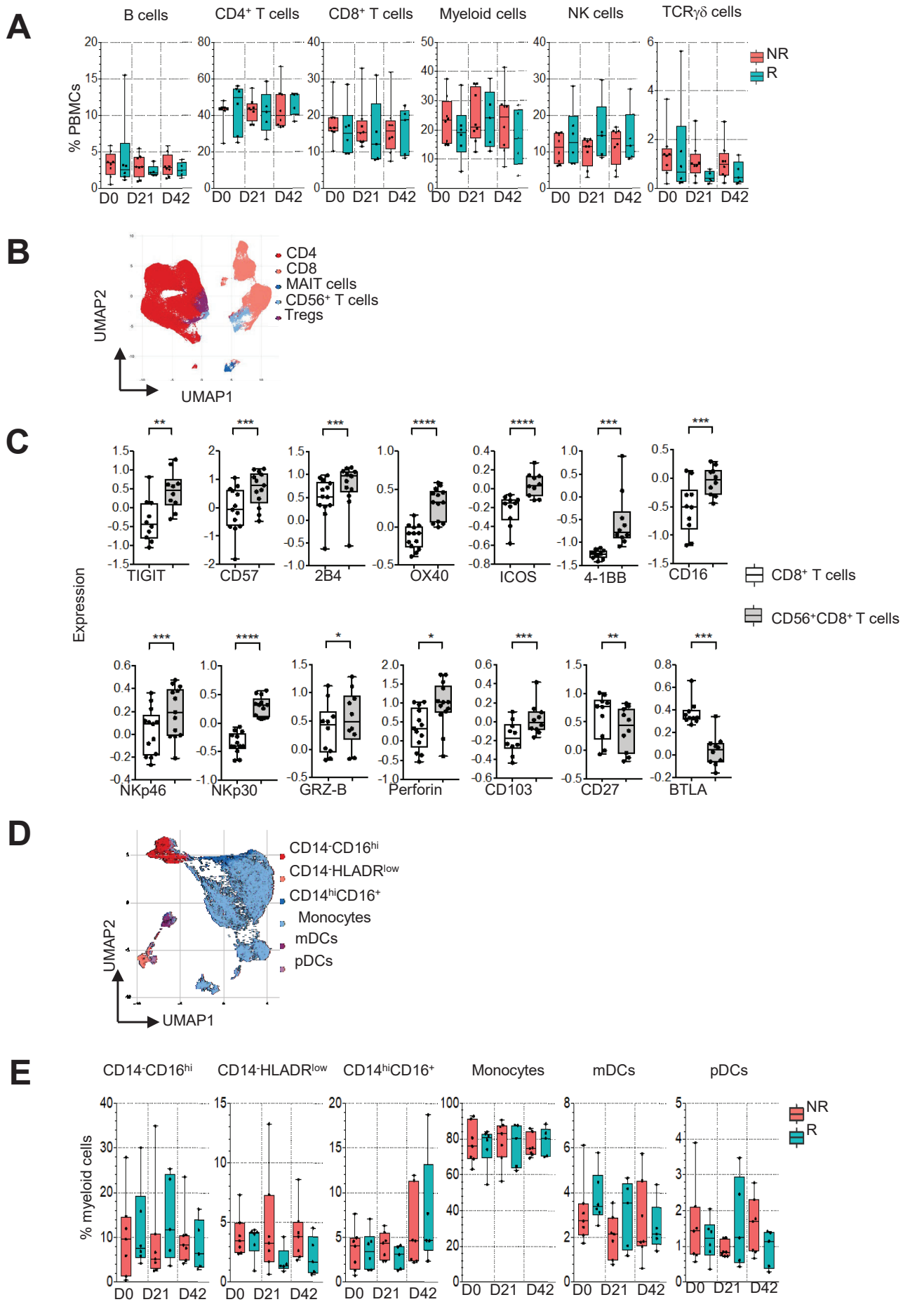
A
B cells
CD4⁺ T cells
CD8⁺ T cells
Myeloid cells
NK cells
TCRγδ cells
% PBMCs
D0 D21 D42
NR
R
B
CD4
CD8
MAIT cells
CD56⁺ T cells
Tregs
UMAP2
UMAP1
C
Expression
TIGIT
CD57
2B4
OX40
ICOS
4-1BB
CD16
NKp46
NKp30
GRZ-B
Perforin
CD103
CD27
BTLA
CD8⁺ T cells
CD56⁺CD8⁺ T cells
D
CD14-CD16hi
CD14-HLADRlow
CD14hiCD16+
Monocytes
mDCs
pDCs
UMAP2
UMAP1
E
CD14-CD16hi
CD14-HLADRlow
CD14hiCD16+
Monocytes
mDCs
pDCs
% myeloid cells
D0 D21 D42
NR
R

Figure S11.
Unsupervised Spectral Flow Cytometry Analysis and Identification of a Highly Activated $CD56^{+}CD8^{+}$ T Cell Subset in the PBMCs of PD-1 Refractory Patients. (A) Whisker boxes showing the frequencies of immune cells in PBMCs between Rs and NRs on day 1 (D1), D21, and D42 after merging clusters based on expression of CD3, CD4, CD8, CD19, CD14, CD56, Tgd1, and Tgd2. Myeloid cells were identified as lineage-negative cell clusters with or without $CD14^{+}$ cells. (B) UMAP visualization of 10,000 events from the $TCRgd^{-}CD3^{+}$ T-cell cluster showing $CD8^{+}$ T cells, $CD4^{+}$ T cells, $CD25^{+}CD127^{-}$ Tregs, $TCRav7.2^{+}CD161^{+}$ MAIT cells, and $CD3^{+}CD56^{+}$ T cells. (C) Comparison of expression (normalized MFI) of the indicated makers by $CD8^{+}$ and $CD56^{+}CD8^{+}$ T-cell clusters pre-treatment from four different flow panels (n=10–14). *P*-values were obtained by parametric or non-parametric paired *t*-tests according to gaussian or non-gaussian distribution of data with: *$p < 0.05$; **$p < 0.01$; ***$p < 0.001$; ****$p < 0.0001$. (D) UMAP visualization of 10,000 events from the myeloid cell subsets showing $CD14^{-}CD11c^{+}HLADR^{+}$ mDCs, $CD123^{+}BDCA2^{+}HLA\text{-}DR^{+}$ pDCs, $CD14^{+}CD16^{hi}$ cells, $CD14^{-}CD16^{+}$ cells, and $CD33^{low}CD14^{-}HLADR^{low}$ myeloid cells. (E) Whisker boxes showing percentages of myeloid cell subsets between Rs and NRs for three time points in the myeloid population. (D and E) $CD3^{+}$, $CD19^{+}$, and $CD33^{-}CD56^{+}$ cells were excluded from the analysis.

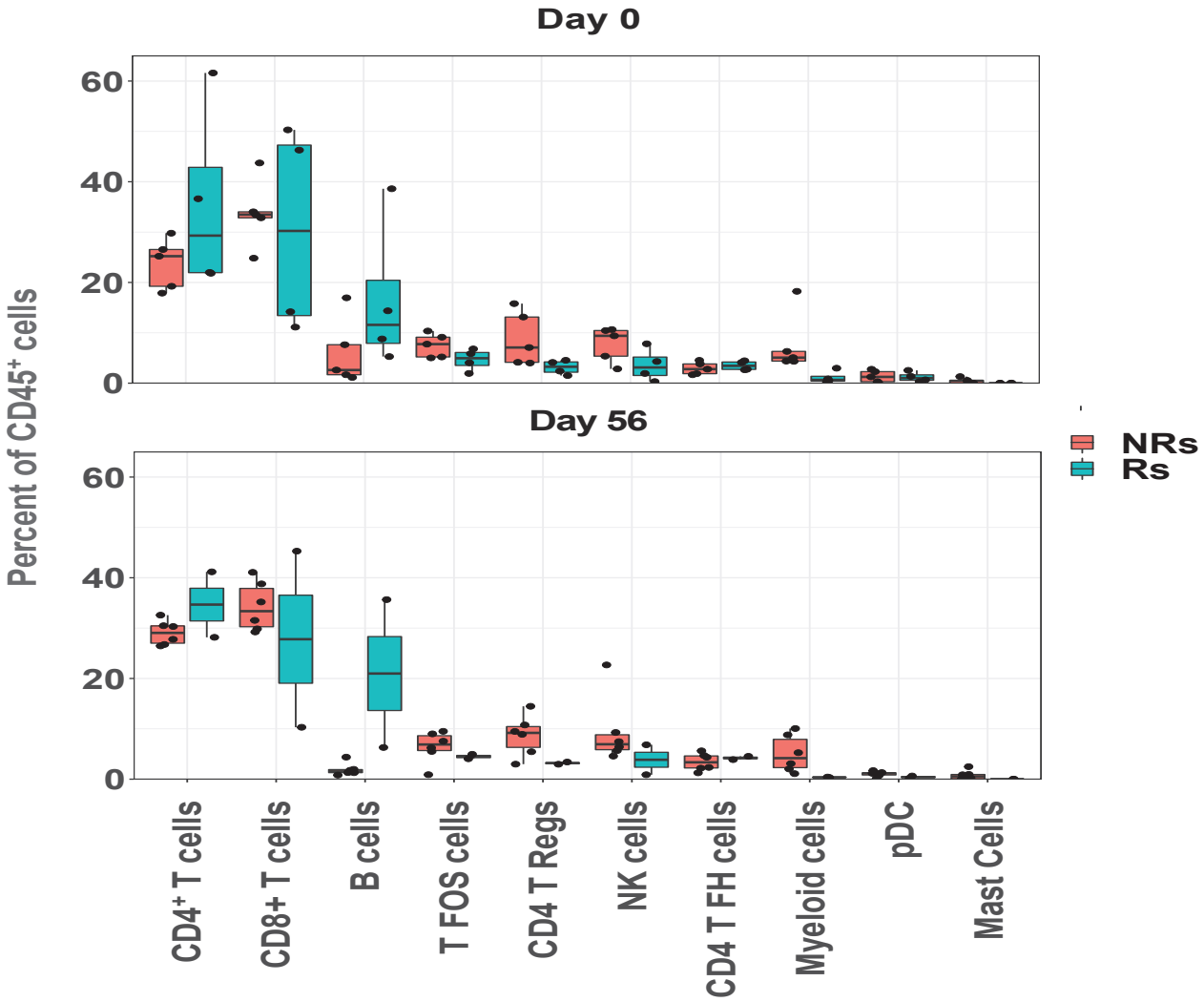

Figure S12.
Abundance of ScRNA-seq Clusters in CD45$^+$ Tumor-Infiltrating Cells. Whisker boxes showing the abundance of each cluster before and after (day 56) treatment in Rs and NRs. Abundance was calculated by dividing the number of cells in a sample by the total number of cells in that sample. *$p < 0.05$.

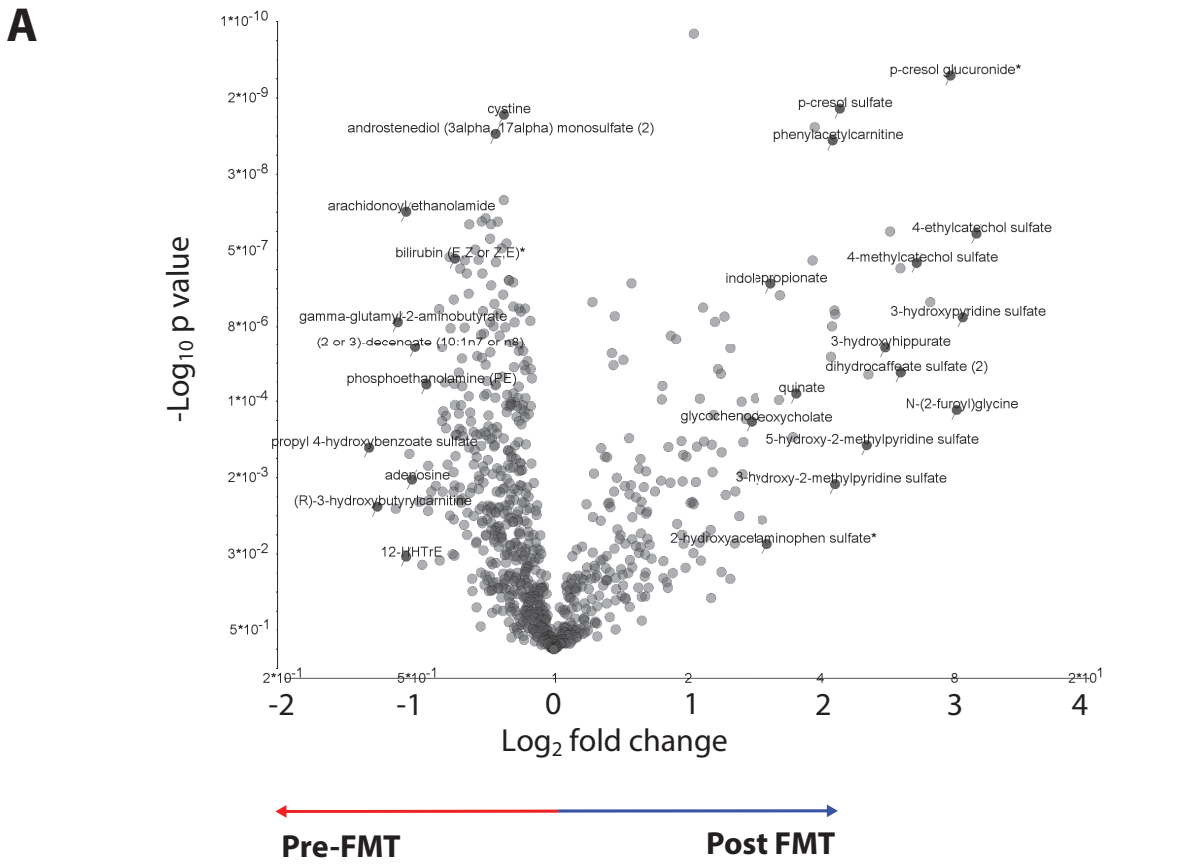
A
-Log10 p value
Log2 fold change
p-cresol glucuronide*
p-cresol sulfate
phenylacetylcarnitine
cystine
androstenediol (3alpha, 17alpha) monosulfate (2)
arachidonoylethanolamide
4-ethylcatechol sulfate
bilirubin (E,Z or Z,E)*
4-methylcatechol sulfate
indolepropionate
3-hydroxypyridine sulfate
gamma-glutamyl-2-aminobutyrate
3-hydroxyhippurate
(2 or 3)-decenoate (10:1n7 or n8)
dihydrocaffeate sulfate (2)
phosphoethanolamine (PE)
quinate
N-(2-furoyl)glycine
glycochenodeoxycholate
propyl 4-hydroxybenzoate sulfate
5-hydroxy-2-methylpyridine sulfate
adenosine
3-hydroxy-2-methylpyridine sulfate
(R)-3-hydroxybutyrylcarnitine
2-hydroxyacetaminophen sulfate*
12-HHTrE
Pre-FMT
Post FMT

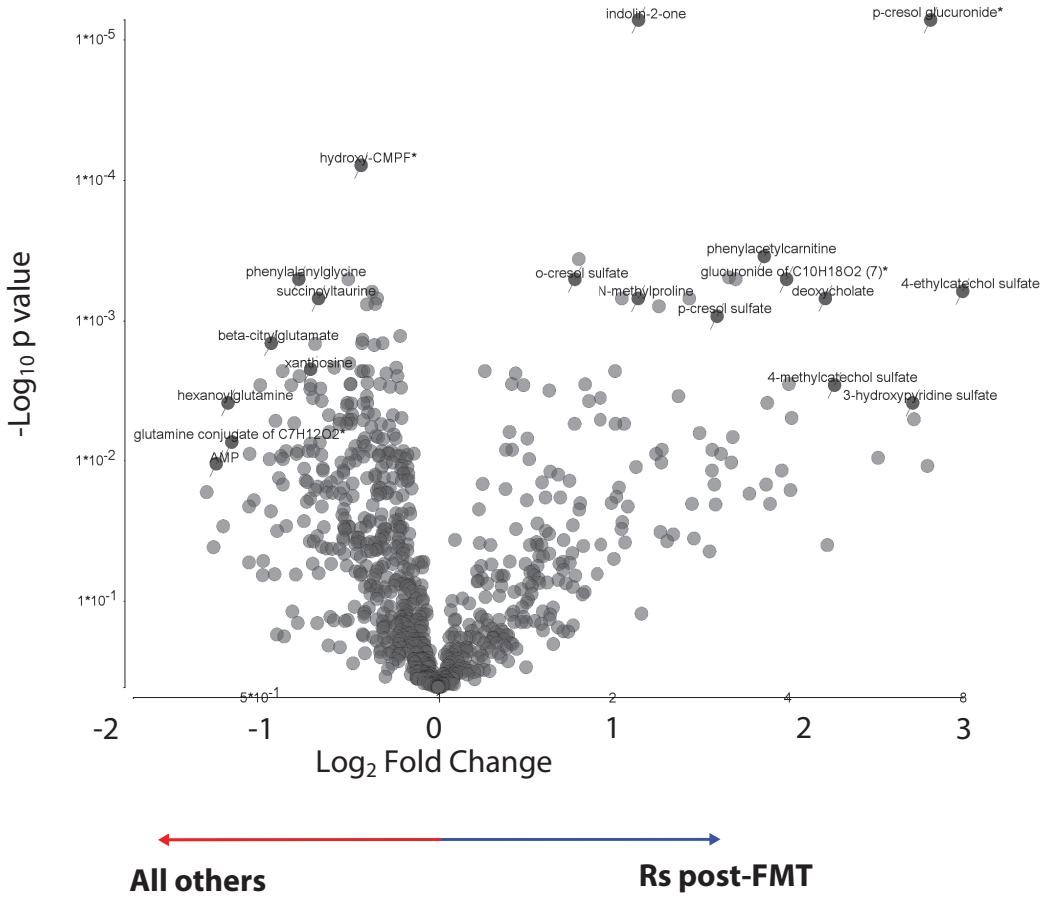
B
-Log10 p value
Log2 Fold Change
indolin-2-one
p-cresol glucuronide*
hydroxy-CMPF*
phenylacetylcarnitine
phenylalanylglycine
o-cresol sulfate
glucuronide of C10H18O2 (7)*
4-ethylcatechol sulfate
succinoyltaurine
N-methylproline
deoxycholate
p-cresol sulfate
beta-citrylglutamate
xanthosine
4-methylcatechol sulfate
hexanoylglutamine
3-hydroxypyridine sulfate
glutamine conjugate of C7H12O2*
AMP
All others
Rs post-FMT

Figure S13.
Relationship Between Serum Metabolites and Outcome in Response to FMT. Volcano plots of inverse $\log^{10}$ p-values and $\log^{2}$ fold change of serum metabolites for A) all patients at pre- and post- FMT time points and B) Rs post-FMT vs all others. Metabolites increased post-transplant in Rs are displayed on the right side of the plots, and those that decreased are shown on the left. Labels of several example metabolites with most significant fold changes and p-values are shown.

Davar et al. Figure S14

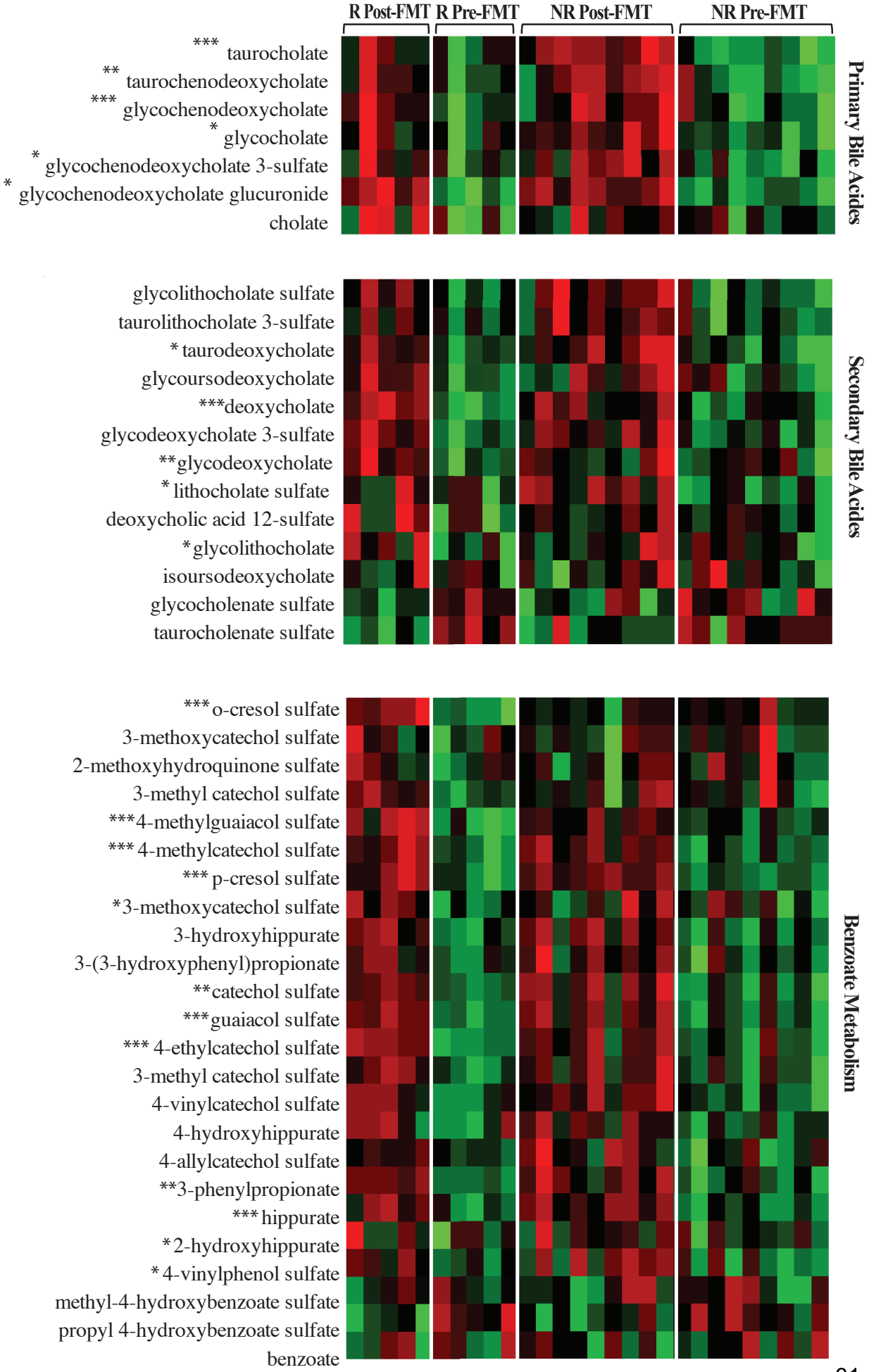

Figure S14.
Visualization of the Selected Significant Metabolic Families in the Serum of Rs and NRs pre- and post-FMT. All detected primary (upper panel) and secondary (middle panel) bile acids, as well as metabolic compounds from benzoate metabolism (lower panel) regardless of significance are plotted as a heatmap. Two-way ANOVA was used to calculate significance and the adjusted p-value results were denoted for $q<0.001$ as ***, $q<0.01$ as ** and $q<0.05$ as *.

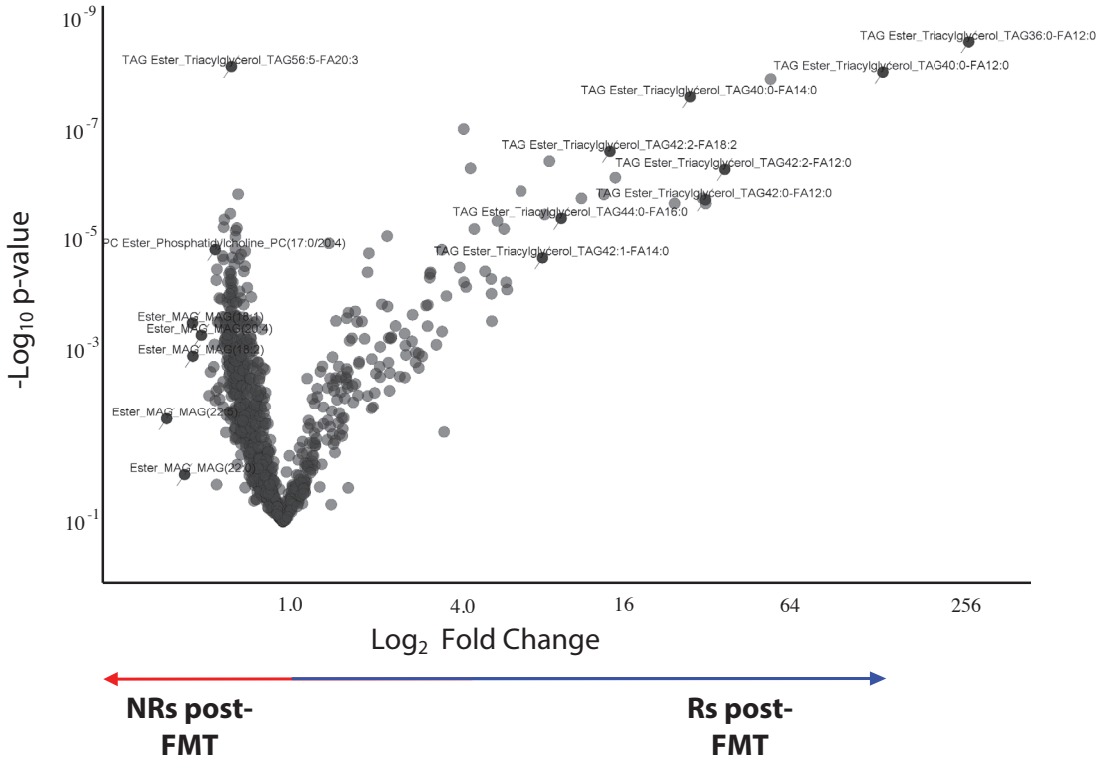

Figure S15.
Relationship Between Serum Lipids and Outcome in Response to FMT/ Pembrolizumab. Lipidomic dataset analysis. Volcano plot of $\log^2$ ratios and p-value of comparison of Rs post-FMT and NRs post-FMT.

Characteristic	Value
Median age, years (range)	61 (35–85)
Sex • Male • Female	 11 (73.3%) 4 (26.7%)
Caucasian ethnicity	15 (100.0%)
Median BMI (range)[#]	27.7 (21.9-55.3)
Neutrophil to lymphocyte ratio (NLR)[#] • Pre-treatment, median (range) • Post-treatment, median (range)	 3.4 (1.4-6.3) 3.9 (1.9-17.3)
ECOG performance status • 0 • 1	 12 (80.0%) 3 (20.0%)
Primary site • Cutaneous • Mucosal • Unknown primary	 13 (86.7%) 1 (6.7%) 2 (13.3%)
Extent of disease • Cutaneous, subcutaneous and/or lymph node metastases • Lung metastases • Visceral metastases (excluding CNS) • Visceral metastases (including treated CNS disease)	 6 (40.0%) 2 (13.3%) 5 (33.3%) 2 (13.3%)
LDH level, (IU/L) • Normal • 1–2x ULN (171) • >2x ULN	 1 (6.7%) 11 (73.3%) 3 (20.0%)
Mutation status • BRAF • NRAS • WT	 4 (26.7%) 3 (20.0%) 8 (53.3%)
Number of prior therapies for metastatic disease • Median • 1 • 2 • ≥3	 2 8 (53.3%) 4 (26.7%) 3 (20.0%)
*Sixteen patients were enrolled, of whom 15 were evaluable (defined as having started therapy and had ≥1 restaging scan). One patient (PT-18-0017) who experienced rapid clinical decline shortly after one cycle of therapy secondary to disease progression was not included in efficacy and microbiome analyses but was evaluable for safety. [#]Testing the effects of BMI, NLR on microbial composition and clinical response revealed no significant effect upon either compositional similarity or diversity in recipients using logistic and linear regression.	

Table S1.
Baseline Patient Demographics and Clinical Characteristics (n=15*)

17-034 Donor ID	Sex	Age (at LFU)	Stage (before anti-PD-1)	Number of Systemic Therapies Before Anti-PD-1	Best Response to Anti-PD-1*	Current Response to Anti-PD-1*	PFS (months)	Current Status
PT-18-0002	M	75	IV-A	1	CR	CR	60	On surveillance
PT-18-0005	F	66	IV-C	1	CR	CR	62	On surveillance
PT-18-0006	F	66	IV-C	0	CR	CR	56	On surveillance
PT-18-0008	M	74	IV-A	0	PR	PR	56	On surveillance
PT-18-0014	M	62	IV-A	0	PR	PR	45	On surveillance
PT-18-0031	F	71	IV-B	0	PR	PR	70	On surveillance
PT-19-0011	M	77	IV-D	0	CR	CR	43	On surveillance
PT-18-0002	M	75	IV-A	1	CR	CR	60	On surveillance

*Response was assessed using RECIST v1.1 by an independent blinded radiologist

Table S2.
Baseline Patient Demographics and Clinical Characteristics of FMT Donors

	Grade 1 (N, %)	Grade 2 (N, %)	Grade 3 (N, %)	Grade 4/5 (N, %)
Constitutional				
Fever	1 (1.6)	0 (0.0)	0 (0.0)	0 (0.0)
Fatigue	6 (9.7)	5 (29.4)	2 (33.3%)	0 (0.0)
Anorexia	2 (3.2)	1 (5.9)	0 (0.0)	0 (0.0)
Weight loss	2 (3.2)	1 (5.9)	0 (0.0)	0 (0.0)
Hematologic				
Anemia	0 (0.0)	1 (5.9)	0 (0.0)	0 (0.0)
Lymphocyte count decrease	1 (1.6)	0 (0.0)	0 (0.0)	0 (0.0)
Platelet count decrease	1 (1.6)	0 (0.0)	0 (0.0)	0 (0.0)
Endocrine				
Adrenal insufficiency	0 (0.0)	0 (0.0)	0 (0.0)	0 (0.0)
Hypothyroidism	3 (4.8)	3 (17.6)	0 (0.0)	0 (0.0)
Dermatologic				
Rash	1 (1.6)	0 (0.0)	0 (0.0)	0 (0.0)
Vitiligo	1 (1.6)	0 (0.0)	0 (0.0)	0 (0.0)
Pruritus	1 (1.6)	1 (5.9)	0 (0.0)	0 (0.0)
Renal and Electrolyte				
Creatinine increase	1 (1.6)	0 (0.0)	0 (0.0)	0 (0.0)
BUN increase	3 (4.8)	0 (0.0)	0 (0.0)	0 (0.0)
Hypokalemia	1 (1.6)	0 (0.0)	0 (0.0)	0 (0.0)
Hyponatremia	10 (16.1)	0 (0.0)	1 (16.7)	0 (0.0)
Hypophosphatemia	2 (3.2)	1 (5.9)	0 (0.0)	0 (0.0)
Hyperphosphatemia	2 (3.2)	0 (0.0)	0 (0.0)	0 (0.0)
Gastrointestinal				
Bloating	14 (22.6)	2 (11.8)	0 (0.0)	0 (0.0)
Nausea and vomiting	1 (1.6)	1 (5.9)	0 (0.0)	0 (0.0)
Aspartate aminotransferase increase	2 (3.2)	0 (0.0)	0 (0.0)	0 (0.0)
Alanine aminotransferase increase	2 (3.2)	0 (0.0)	0 (0.0)	0 (0.0)
Alkaline phosphatase increase	1 (1.6)	0 (0.0)	0 (0.0)	0 (0.0)
Total bilirubin increase	1 (1.6)	0 (0.0)	0 (0.0)	0 (0.0)
Albumin decrease	2 (3.2)	0 (0.0)	0 (0.0)	0 (0.0)
Diarrhea (non-colitis)	1 (1.6)	1 (5.9)	0 (0.0)	0 (0.0)
Neurologic				
Fatigue	0 (0.0)	0 (0.0)	2 (33.3)	0 (0.0)
Peripheral motor neuropathy	0 (0.0)	0 (0.0)	1 (16.7)	0 (0.0)

Table S3.
Summary of Adverse Events in the FMT/Pembrolizumab Clinical Trial (n=16)

CD4 T	CD8 T	CD4 T Regs	CD4 T FH	T FOS	NK	B	Myeloid	pDC	Mast Cells
IL7R	*CCL5*	*FOXP3*	*CXCL13*	*EGR1*	*GNLY*	*CD79A*	*CST3*	*PTGDS*	*TPSAB1*
CCR7	*CD8A*	*BATF*	*NMB*	*GADD45B*	*FGFBP2*	*IGKC*	*LYZ*	*PLD4*	*TPSB2*
ANXA1	*GZMK*	*CARD16*	*NR3C1*	*JUN*	*SPON2*	*MS4A1*	*IFI30*	*SOX4*	*CPA3*
S1PR1	*LAG3*	*TIGIT*	*TOX2*	*TNF*	*PRF1*	*HLA-DRA*	*S100A8*	*LILRA4*	*HPGD*
KLF2	*CD8B*	*IL32*	*IGFBP4*	*FOS*	*GZMB*	*CD83*	*SPP1*	*IRF7*	*CLU*
LEF1	*GZMA*	*TNFRSF4*	*ITM2A*	*CITED2*	*KLRF1*	*HLA-DQB1*	*TIMP1*	*TCF4*	*HPGDS*
TCF7	*GZMH*	*TNFRSF18*	*CD200*	*HSPA1B*	*KLRD1*	*CD74*	*CXCL8*	*IRF8*	*CD9*
LTB	*NKG7*	*IL2RA*	*MAGEH1*	*IER2*	*FCGR3A*	*HLA-DRB5*	*APOE*	*GPR183*	*GATA2*
FLT3LG	*CST7*	*TBC1D4*	*DUSP4*	*FOSB*	*NKG7*	*HLA-DQA1*	*C1QC*	*SERPINF1*	*VWA5A*
GIMAP7	*DUSP2*	*CTLA4*	*TNFRSF4*	*UBE2S*	*FCER1G*	*HLA-DPA1*	*C1QB*	*ITM2C*	*PRG2*
MAL	*CCL4*	*ARID5B*	*FKBP5*	*DUSP1*	*KLRB1*	*MEF2C*	*S100A9*	*IL3RA*	*TPSD1*
AQP3	*PTMS*	*CXCR6*	*PDCD1*	*ID2*	*CTSW*	*IGHM*	*C1QA*	*NPC2*	*LTC4S*
NOSIP	*KLRK1*	*LINC01943*	*TSHZ2*	*H2AFX*	*HOPX*	*FCER2*	*TYROBP*	*GZMB*	*SLC18A2*
LDHB	*RGS1*	*ICOS*	*GK*	*SNHG12*	*CLIC3*	*HLA-DRB1*	*FTL*	*CCDC50*	*HDC*
CD55	*COTL1*	*RTKN2*	*RNF19A*	*NR4A1*	*XCL2*	*CD19*	*FCER1G*	*CST3*	*CTSG*
RPL32	*CRTAM*	*GLRX*	*CORO1B*	*DNAJB1*	*EFHD2*	*CD79B*	*AIF1*	*APP*	*KIT*
RPS12	*FABP5*	*PBXIP1*	*LIMS1*	*IER3*	*CCL4*	*HLA-DPB1*	*PLAUR*	*SPIB*	*BACE2*
TPT1	*PDCD1*	*LAYN*	*TOX*	*NEU1*	*TRDC*	*HERPUD1*	*CTSL*	*IRF4*	*RHEX*
ARRDC2	*ITM2A*	*LTB*	*PASK*	*IER5*	*ADGRG1*	*VPREB3*	*IFITM3*	*JCHAIN*	*AL157895.1*
FXYD5	*APOBEC3G*	*STAM*	*CD4*	*SERTAD1*	*CX3CR1*	*ID3*	*CD68*	*SEC61B*	*IL1RL1*
RPL5	*IFNG*	*PIM2*	*SH2D1A*	*RSRP1*	*SH2D1B*	*SMIM14*	*PSAP*	*UGCG*	*SIGLEC6*
SELL	*CD27*	*IKZF2*	*MAF*	*SRSF7*	*XCL1*	*NR4A1*	*CD14*	*TSPAN13*	*RAB32*
SATB1	*TNFSF9*	*CORO1B*	*ZNRF1*	*JUNB*	*CD247*	*HLA-DMA*	*CTSB*	*SCT*	*PTGS1*
RPS3A	*LYST*	*RGS1*	*SPOCK2*	*PPP1R15A*	*S1PR5*	*CD37*	*CCL2*	*PLAC8*	*RHOBTB3*
RPS13	*GZMB*	*TNFRSF1B*	*PHACTR2*	*UBB*	*AREG*	*BASP1*	*C15orf48*	*CLIC3*	*CNRIP1*
EEF1A1	*CD3D*	*AC017002.3*	*FAAH2*	*H3F3B*	*CST7*	*SPIB*	*FCN1*	*MPEG1*	*MAOB*
KLF3	*DUSP5*	*S100A4*	*ICOS*	*ZFP36L1*	*CCL3*	*HVCN1*	*SERPINA1*	*GRN*	*GCSAML*
CAMK4	*PLAAT4*	*GBP5*	*SRGN*	*HSPA1A*	*IL2RB*	*LY9*	*CXCL2*	*SMPD3*	*STXBP6*
RPL3	*CD2*	*UGP2*	*TNIK*	*SAP18*	*KLRC1*	*ARHGAP24*	*SPI1*	*TPM2*	*GMPR*
GAS5	*CYTOR*	*CYTOR*	*ARID5B*	*TUBA1B*	*MATK*	*RALGPS2*	*G0S2*	*TCL1A*	*NTRK1*
RPL34	*CTSW*	*DUSP4*	*COTL1*	*HSPA8*	*PLAC8*	*NCF1*	*HLA-DRA*	*CYB561A3*	*TIMP3*
EEF1B2	*CXCR6*	*IL12RB2*	*LAT*	*FUS*	*MAFF*	*CD40*	*SOD2*	*LRRC26*	*SLC45A3*
RPS6	*PRF1*	*DNPH1*	*FYN*	*EIF4A3*	*CMC1*	*CXCR5*	*IER3*	*TRAF4*	*RGS13*
RPL13	*HCST*	*CD2*	*SESN3*	*HIST2H2AA4*	*GZMH*	*LY86*	*CXCL3*	*CD74*	*HS3ST1*
RPS14	*TENT5C*	*GK*	*HNRNPLL*	*HEXIM1*	*IFITM2*	*SNX2*	*NPC2*	*DERL3*	*PMP22*
RPL14	*CMC1*	*SPOCK2*	*TNFRSF18*	*EIF4A2*	*TTC38*	*CD22*	*IFI27*	*FCER1G*	*FCER1G*
RPL36	*CLEC2B*	*DUSP16*	*IL6ST*	*CD69*	*CEBPD*	*LYN*	*LST1*	*MZB1*	*TMEM176B*
SARAF	*IL32*	*NCF4*	*TCF7*	*MARCKSL1*	*FGR*	*EZR*	*HLA-DRB1*	*CLEC4C*	*ALOX5*
RPL4	*CD3E*	*HLA-A*	*TBC1D4*	*MYLIP*	*FOSL2*	*SYNGR2*	*S100A11*	*EGLN3*	*CST3*
GIMAP5	*RUNX3*	*B2M*	*FYB1*	*DNAJA1*	*MAP3K8*	*BLK*	*SAT1*	*LDLRAD4*	*RAB27B*
GPR183	*TIGIT*	*HTATIP2*	*BATF*	*SRSF2*	*TBX21*	*FCRLA*	*CCL3*	*TYROBP*	*IFITM3*
RPL11	*CXCR3*	*CASP1*	*CTLA4*	*TUBB2A*	*PTGDR*	*ADAM28*	*GRN*	*LILRB4*	*ACSL4*
RPS3	*IDH2*	*RPS27L*	*LINC00963*	*BRD2*	*CD300A*	*LINC00926*	*IL1RN*	*RNASE6*	*STX3*
EEF1G	*PTPRCAP*	*CTSC*	*CNIH1*	*TUBA1A*	*ITGB2*	*CD24*	*CTSD*	*RASD1*	*BTK*
RPLP0	*GZMM*	*FAS*	*SARAF*	*TXNIP*	*PLEK*	*SWAP70*	*MS4A6A*	*PTCRA*	*ABCC4*
RPS8	*RAB27A*	*GBP2*	*SOD1*	*SNHG5*	*ABHD17A*	*HSP90AB1*	*HLA-DPA1*	*KRT5*	*GLUL*
RPL9	*SH2D1A*	*MAF*	*PLIN2*	*PNP*	*KLRK1*	*FCRL1*	*MAFB*	*C12orf75*	*HES1*
RPL36A	*SRRT*	*SOD1*	*TGIF1*	*HSP90AA1*	*GZMA*	*HLA-DMB*	*HLA-DPB1*	*GAS6*	*SLC44A1*
RPL22	*FYN*	*TMEM173*	*SLA*	*SNHG1*	*GZMM*	*AFF3*	*BCL2A1*	*DNASE1L3*	*SOX4*

Table S4.
Top 50 Differentially Expressed Genes in Combined Clusters in scRNA-seq Analyses

References and Notes

1. J. Larkin, C. D. Lao, W. J. Urba, D. F. McDermott, C. Horak, J. Jiang, J. D. Wolchok, Efficacy and safety of nivolumab in patients with BRAF V600 mutant and BRAF wild-type advanced melanoma: A pooled analysis of 4 clinical trials. *JAMA Oncol.* **1**, 433–440 (2015). doi:10.1001/jamaoncol.2015.1184 Medline

2. A. Ribas, O. Hamid, A. Daud, F. S. Hodi, J. D. Wolchok, R. Kefford, A. M. Joshua, A. Patnaik, W. J. Hwu, J. S. Weber, T. C. Gangadhar, P. Hersey, R. Dronca, R. W. Joseph, H. Zarour, B. Chmielowski, D. P. Lawrence, A. Algazi, N. A. Rizvi, B. Hoffner, C. Mateus, K. Gergich, J. A. Lindia, M. Giannotti, X. N. Li, S. Ebbinghaus, S. P. Kang, C. Robert, Association of pembrolizumab with tumor response and survival among patients with advanced melanoma. *JAMA* **315**, 1600–1609 (2016). doi:10.1001/jama.2016.4059 Medline

3. C. Robert, G. V. Long, B. Brady, C. Dutriaux, M. Maio, L. Mortier, J. C. Hassel, P. Rutkowski, C. McNeil, E. Kalinka-Warzocha, K. J. Savage, M. M. Hernberg, C. Lebbé, J. Charles, C. Mihalcioiu, V. Chiarion-Sileni, C. Mauch, F. Cognetti, A. Arance, H. Schmidt, D. Schadendorf, H. Gogas, L. Lundgren-Eriksson, C. Horak, B. Sharkey, I. M. Waxman, V. Atkinson, P. A. Ascierto, Nivolumab in previously untreated melanoma without BRAF mutation. *N. Engl. J. Med.* **372**, 320–330 (2015). doi:10.1056/NEJMoa1412082 Medline

4. C. Robert, A. Ribas, J. Schachter, A. Arance, J. J. Grob, L. Mortier, A. Daud, M. S. Carlino, C. M. McNeil, M. Lotem, J. M. G. Larkin, P. Lorigan, B. Neyns, C. U. Blank, T. M. Petrella, O. Hamid, S. C. Su, C. Krepler, N. Ibrahim, G. V. Long, Pembrolizumab versus ipilimumab in advanced melanoma (KEYNOTE-006): Post-hoc 5-year results from an open-label, multicentre, randomised, controlled, phase 3 study. *Lancet Oncol.* **20**, 1239–1251 (2019). doi:10.1016/S1470-2045(19)30388-2 Medline

5. C. Robert, J. Schachter, G. V. Long, A. Arance, J. J. Grob, L. Mortier, A. Daud, M. S. Carlino, C. McNeil, M. Lotem, J. Larkin, P. Lorigan, B. Neyns, C. U. Blank, O. Hamid, C. Mateus, R. Shapira-Frommer, M. Kosh, H. Zhou, N. Ibrahim, S. Ebbinghaus, A. Ribas, KEYNOTE-006 investigators, Pembrolizumab versus ipilimumab in advanced melanoma. *N. Engl. J. Med.* **372**, 2521–2532 (2015). doi:10.1056/NEJMoa1503093 Medline

6. A. Dzutsev, R. S. Goldszmid, S. Viaud, L. Zitvogel, G. Trinchieri, The role of the microbiota in inflammation, carcinogenesis, and cancer therapy. *Eur. J. Immunol.* **45**, 17–31 (2015). doi:10.1002/eji.201444972 Medline

7. B. B. Finlay, R. Goldszmid, K. Honda, G. Trinchieri, J. Wargo, L. Zitvogel, Can we harness the microbiota to enhance the efficacy of cancer immunotherapy? *Nat. Rev. Immunol.* **20**, 522–528 (2020). doi:10.1038/s41577-020-0374-6 Medline

8. R. S. Goldszmid, A. Dzutsev, S. Viaud, L. Zitvogel, N. P. Restifo, G. Trinchieri, Microbiota modulation of myeloid cells in cancer therapy. *Cancer Immunol. Res.* **3**, 103–109 (2015). doi:10.1158/2326-6066.CIR-14-0225 Medline

9. H. M. Zarour, Reversing T-cell dysfunction and exhaustion in cancer. *Clin. Cancer Res.* **22**, 1856–1864 (2016). doi:10.1158/1078-0432.CCR-15-1849 Medline

10. V. Gopalakrishnan, C. N. Spencer, L. Nezi, A. Reuben, M. C. Andrews, T. V. Karpinets, P. A. Prieto, D. Vicente, K. Hoffman, S. C. Wei, A. P. Cogdill, L. Zhao, C. W. Hudgens, D. S. Hutchinson, T. Manzo, M. Petaccia de Macedo, T. Cotechini, T. Kumar, W. S. Chen, S. M. Reddy, R. Szczepaniak Sloane, J. Galloway-Pena, H. Jiang, P. L. Chen, E. J. Shpall, K. Rezvani, A. M. Alousi, R. F. Chemaly, S. Shelburne, L. M. Vence, P. C. Okhuysen, V. B. Jensen, A. G. Swennes, F. McAllister, E. Marcelo Riquelme Sanchez, Y. Zhang, E. Le Chatelier, L. Zitvogel, N. Pons, J. L. Austin-Breneman, L. E. Haydu, E. M. Burton, J. M. Gardner, E. Sirmans, J. Hu, A. J. Lazar, T. Tsujikawa, A. Diab, H. Tawbi, I. C. Glitza, W. J. Hwu, S. P. Patel, S. E. Woodman, R. N. Amaria, M. A. Davies, J. E. Gershenwald, P. Hwu, J. E. Lee, J. Zhang, L. M. Coussens, Z. A. Cooper, P. A. Futreal, C. R. Daniel, N. J. Ajami, J. F. Petrosino, M. T. Tetzlaff, P. Sharma, J. P. Allison, R. R. Jenq, J. A. Wargo, Gut microbiome modulates response to anti-PD-1 immunotherapy in melanoma patients. *Science* **359**, 97–103 (2018). doi:10.1126/science.aan4236 Medline

11. V. Matson, J. Fessler, R. Bao, T. Chongsuwat, Y. Zha, M. L. Alegre, J. J. Luke, T. F. Gajewski, The commensal microbiome is associated with anti-PD-1 efficacy in metastatic melanoma patients. *Science* **359**, 104–108 (2018). doi:10.1126/science.aao3290 Medline

12. B. Routy, E. Le Chatelier, L. Derosa, C. P. M. Duong, M. T. Alou, R. Daillère, A. Fluckiger, M. Messaoudene, C. Rauber, M. P. Roberti, M. Fidelle, C. Flament, V. Poirier-Colame, P. Opolon, C. Klein, K. Iribarren, L. Mondragón, N. Jacquelot, B. Qu, G. Ferrere, C. Clémenson, L. Mezquita, J. R. Masip, C. Naltet, S. Brosseau, C. Kaderbhai, C. Richard, H. Rizvi, F. Levenez, N. Galleron, B. Quinquis, N. Pons, B. Ryffel, V. Minard-Colin, P. Gonin, J. C. Soria, E. Deutsch, Y. Loriot, F. Ghiringhelli, G. Zalcman, F. Goldwasser, B. Escudier, M. D. Hellmann, A. Eggermont, D. Raoult, L. Albiges, G. Kroemer, L. Zitvogel, Gut microbiome influences efficacy of PD-1-based immunotherapy against epithelial tumors. *Science* **359**, 91–97 (2018). doi:10.1126/science.aan3706 Medline

13. A. E. Frankel, L. A. Coughlin, J. Kim, T. W. Froehlich, Y. Xie, E. P. Frenkel, A. Y. Koh, Metagenomic shotgun sequencing and unbiased metabolomic profiling identify specific human gut microbiota and metabolites associated with immune checkpoint therapy efficacy in melanoma patients. *Neoplasia* **19**, 848–855 (2017). doi:10.1016/j.neo.2017.08.004 Medline

14. B. A. Peters, M. Wilson, U. Moran, A. Pavlick, A. Izsak, T. Wechter, J. S. Weber, I. Osman, J. Ahn, Relating the gut metagenome and metatranscriptome to immunotherapy responses in melanoma patients. *Genome Med.* **11**, 61 (2019). doi:10.1186/s13073-019-0672-4 Medline

15. E. A. Eisenhauer, P. Therasse, J. Bogaerts, L. H. Schwartz, D. Sargent, R. Ford, J. Dancey, S. Arbuck, S. Gwyther, M. Mooney, L. Rubinstein, L. Shankar, L. Dodd, R. Kaplan, D. Lacombe, J. Verweij, New response evaluation criteria in solid tumours: Revised RECIST guideline (version 1.1). *Eur. J. Cancer* **45**, 228–247 (2009). doi:10.1016/j.ejca.2008.10.026 Medline

16. H. M. Kluger, H. A. Tawbi, M. L. Ascierto, M. Bowden, M. K. Callahan, E. Cha, H. X. Chen, C. G. Drake, D. M. Feltquate, R. L. Ferris, J. L. Gulley, S. Gupta, R. W. Humphrey, T. M. LaVallee, D. T. Le, V. M. Hubbard-Lucey, V. A.

Papadimitrakopoulou, M. A. Postow, E. H. Rubin, E. Sharon, J. M. Taube, S. L. Topalian, R. Zappasodi, M. Sznol, R. J. Sullivan, Defining tumor resistance to PD-1 pathway blockade: Recommendations from the first meeting of the SITC Immunotherapy Resistance Taskforce. *J. Immunother. Cancer* **8**, e000398 (2020). Medline

17. A. Ribas, J. M. Kirkwood, K. T. Flaherty, Anti-PD-1 antibody treatment for melanoma. *Lancet Oncol.* **19**, e219 (2018). doi:10.1016/S1470-2045(18)30202-X Medline

18. M. Y. Zeng, D. Cisalpino, S. Varadarajan, J. Hellman, H. S. Warren, M. Cascalho, N. Inohara, G. Núñez, Gut microbiota-induced immunoglobulin G controls systemic infection by symbiotic bacteria and pathogens. *Immunity* **44**, 647–658 (2016). doi:10.1016/j.immuni.2016.02.006 Medline

19. D. J. Pinato, S. Howlett, D. Ottaviani, H. Urus, A. Patel, T. Mineo, C. Brock, D. Power, O. Hatcher, A. Falconer, M. Ingle, A. Brown, D. Gujral, S. Partridge, N. Sarwar, M. Gonzalez, M. Bendle, C. Lewanski, T. Newsom-Davis, E. Allara, M. Bower, Association of prior antibiotic treatment with survival and response to immune checkpoint inhibitor therapy in patients with cancer. *JAMA Oncol.* **5**, 1774–1778 (2019). doi:10.1001/jamaoncol.2019.2785 Medline

20. C. Krieg, M. Nowicka, S. Guglietta, S. Schindler, F. J. Hartmann, L. M. Weber, R. Dummer, M. D. Robinson, M. P. Levesque, B. Becher, High-dimensional single-cell analysis predicts response to anti-PD-1 immunotherapy. *Nat. Med.* **24**, 144–153 (2018). doi:10.1038/nm.4466 Medline

21. M. Nowicka, C. Krieg, H. L. Crowell, L. M. Weber, F. J. Hartmann, S. Guglietta, B. Becher, M. P. Levesque, M. D. Robinson, CyTOF workflow: Differential discovery in high-throughput high-dimensional cytometry datasets. *F1000Res.* **6**, 748 (2017). doi:10.12688/f1000research.11622.1 Medline

22. M. J. Pittet, D. E. Speiser, D. Valmori, J. C. Cerottini, P. Romero, Cutting edge: Cytolytic effector function in human circulating $CD8^+$ T cells closely correlates with CD56 surface expression. *J. Immunol.* **164**, 1148–1152 (2000). doi:10.4049/jimmunol.164.3.1148 Medline

23. T. Ohkawa, S. Seki, H. Dobashi, Y. Koike, Y. Habu, K. Ami, H. Hiraide, I. Sekine, Systematic characterization of human $CD8^+$ T cells with natural killer cell markers in comparison with natural killer cells and normal $CD8^+$ T cells. *Immunology* **103**, 281–290 (2001). doi:10.1046/j.1365-2567.2001.01248.x Medline

24. S. Guia, C. Cognet, L. de Beaucoudrey, M. S. Tessmer, E. Jouanguy, C. Berger, O. Filipe-Santos, J. Feinberg, Y. Camcioglu, J. Levy, S. Al Jumaah, S. Al-Hajjar, J. L. Stephan, C. Fieschi, L. Abel, L. Brossay, J. L. Casanova, E. Vivier, A role for interleukin-12/23 in the maturation of human natural killer and $CD56^+$ T cells in vivo. *Blood* **111**, 5008–5016 (2008). doi:10.1182/blood-2007-11-122259 Medline

25. K. Hasumi, Y. Aoki, R. Wantanabe, D. L. Mann, Clinical response of advanced cancer patients to cellular immunotherapy and intensity-modulated radiation therapy. *OncoImmunology* **2**, e26381 (2013). doi:10.4161/onci.26381 Medline

26. A. Ribas, D. S. Shin, J. Zaretsky, J. Frederiksen, A. Cornish, E. Avramis, E. Seja, C. Kivork, J. Siebert, P. Kaplan-Lefko, X. Wang, B. Chmielowski, J. A. Glaspy, P. C. Tumeh, T.

Chodon, D. Pe'er, B. Comin-Anduix, PD-1 blockade expands intratumoral memory T cells. *Cancer Immunol. Res.* **4**, 194–203 (2016). doi:10.1158/2326-6066.CIR-15-0210 Medline

27. A. O. Kamphorst, R. N. Pillai, S. Yang, T. H. Nasti, R. S. Akondy, A. Wieland, G. L. Sica, K. Yu, L. Koenig, N. T. Patel, M. Behera, H. Wu, M. McCausland, Z. Chen, C. Zhang, F. R. Khuri, T. K. Owonikoko, R. Ahmed, S. S. Ramalingam, Proliferation of PD-1^+ CD8 T cells in peripheral blood after PD-1-targeted therapy in lung cancer patients. *Proc. Natl. Acad. Sci. U.S.A.* **114**, 4993–4998 (2017). doi:10.1073/pnas.1705327114 Medline

28. A. Kunert, E. A. Basak, D. P. Hurkmans, H. E. Balcioglu, Y. Klaver, M. van Brakel, A. A. M. Oostvogels, C. H. J. Lamers, S. Bins, S. L. W. Koolen, A. A. M. van der Veldt, S. Sleijfer, R. H. J. Mathijssen, J. G. J. V. Aerts, R. Debets, $CD45RA^+CCR7^-$ CD8 T cells lacking co-stimulatory receptors demonstrate enhanced frequency in peripheral blood of NSCLC patients responding to nivolumab. *J. Immunother. Cancer* **7**, 149 (2019). doi:10.1186/s40425-019-0608-y Medline

29. T. Stuart, A. Butler, P. Hoffman, C. Hafemeister, E. Papalexi, W. M. Mauck III, Y. Hao, M. Stoeckius, P. Smibert, R. Satija, Comprehensive integration of single-cell data. *Cell* **177**, 1888–1902.e21 (2019). doi:10.1016/j.cell.2019.05.031 Medline

30. K. A. Schalper, M. Carleton, M. Zhou, T. Chen, Y. Feng, S. P. Huang, A. M. Walsh, V. Baxi, D. Pandya, T. Baradet, D. Locke, Q. Wu, T. P. Reilly, P. Phillips, V. Nagineni, N. Gianino, J. Gu, H. Zhao, J. L. Perez-Gracia, M. F. Sanmamed, I. Melero, Elevated serum interleukin-8 is associated with enhanced intratumor neutrophils and reduced clinical benefit of immune-checkpoint inhibitors. *Nat. Med.* **26**, 688–692 (2020). doi:10.1038/s41591-020-0856-x Medline

31. H. Alshetaiwi, N. Pervolarakis, L. L. McIntyre, D. Ma, Q. Nguyen, J. A. Rath, K. Nee, G. Hernandez, K. Evans, L. Torosian, A. Silva, C. Walsh, K. Kessenbrock, Defining the emergence of myeloid-derived suppressor cells in breast cancer using single-cell transcriptomics. *Sci. Immunol.* **5**, eaay6017 (2020). doi:10.1126/sciimmunol.aay6017 Medline

32. B. Gok Yavuz, G. Gunaydin, M. E. Gedik, K. Kosemehmetoglu, D. Karakoc, F. Ozgur, D. Guc, Cancer associated fibroblasts sculpt tumour microenvironment by recruiting monocytes and inducing immunosuppressive PD-1^+ TAMs. *Sci. Rep.* **9**, 3172 (2019). doi:10.1038/s41598-019-39553-z Medline

33. M. Terme, E. Ullrich, L. Aymeric, K. Meinhardt, M. Desbois, N. Delahaye, S. Viaud, B. Ryffel, H. Yagita, G. Kaplanski, A. Prévost-Blondel, M. Kato, J. L. Schultze, E. Tartour, G. Kroemer, N. Chaput, L. Zitvogel, IL-18 induces PD-1-dependent immunosuppression in cancer. *Cancer Res.* **71**, 5393–5399 (2011). doi:10.1158/0008-5472.CAN-11-0993 Medline

34. J. L. Benci, B. Xu, Y. Qiu, T. J. Wu, H. Dada, C. Twyman-Saint Victor, L. Cucolo, D. S. M. Lee, K. E. Pauken, A. C. Huang, T. C. Gangadhar, R. K. Amaravadi, L. M. Schuchter, M. D. Feldman, H. Ishwaran, R. H. Vonderheide, A. Maity, E. J. Wherry, A. J. Minn, Tumor interferon signaling regulates a multigenic resistance program to immune checkpoint blockade. *Cell* **167**, 1540–1554.e12 (2016). doi:10.1016/j.cell.2016.11.022 Medline

35. M. Danilo, V. Chennupati, J. G. Silva, S. Siegert, W. Held, Suppression of Tcf1 by inflammatory cytokines facilitates effector CD8 T cell differentiation. *Cell Rep.* **22**, 2107–2117 (2018). doi:10.1016/j.celrep.2018.01.072 Medline

36. H. K. Koblish, C. A. Hunter, M. Wysocka, G. Trinchieri, W. M. Lee, Immune suppression by recombinant interleukin (rIL)-12 involves interferon gamma induction of nitric oxide synthase 2 (iNOS) activity: Inhibitors of NO generation reveal the extent of rIL-12 vaccine adjuvant effect. *J. Exp. Med.* **188**, 1603–1610 (1998). doi:10.1084/jem.188.9.1603 Medline

37. M. F. Sanmamed, J. L. Perez-Gracia, K. A. Schalper, J. P. Fusco, A. Gonzalez, M. E. Rodriguez-Ruiz, C. Oñate, G. Perez, C. Alfaro, S. Martín-Algarra, M. P. Andueza, A. Gurpide, M. Morgado, J. Wang, A. Bacchiocchi, R. Halaban, H. Kluger, L. Chen, M. Sznol, I. Melero, Changes in serum interleukin-8 (IL-8) levels reflect and predict response to anti-PD-1 treatment in melanoma and non-small-cell lung cancer patients. *Ann. Oncol.* **28**, 1988–1995 (2017). doi:10.1093/annonc/mdx190 Medline

38. P. Vernocchi, F. Del Chierico, L. Putignani, Gut microbiota profiling: Metabolomics based approach to unravel compounds affecting human health. *Front. Microbiol.* **7**, 1144 (2016). doi:10.3389/fmicb.2016.01144 Medline

39. T. Pallister, M. A. Jackson, T. C. Martin, J. Zierer, A. Jennings, R. P. Mohney, A. MacGregor, C. J. Steves, A. Cassidy, T. D. Spector, C. Menni, Hippurate as a metabolomic marker of gut microbiome diversity: Modulation by diet and relationship to metabolic syndrome. *Sci. Rep.* **7**, 13670 (2017). doi:10.1038/s41598-017-13722-4 Medline

40. K. Martinez-Guryn, N. Hubert, K. Frazier, S. Urlass, M. W. Musch, P. Ojeda, J. F. Pierre, J. Miyoshi, T. J. Sontag, C. M. Cham, C. A. Reardon, V. Leone, E. B. Chang, Small intestine microbiota regulate host digestive and absorptive adaptive responses to dietary lipids. *Cell Host Microbe* **23**, 458–469.e5 (2018). doi:10.1016/j.chom.2018.03.011 Medline

41. R. R. Rodrigues, N. Shulzhenko, A. Morgun, Transkingdom networks: A systems biology approach to identify causal members of host-microbiota interactions. *Methods Mol. Biol.* **1849**, 227–242 (2018). doi:10.1007/978-1-4939-8728-3_15 Medline

42. A. Yambartsev, M. A. Perlin, Y. Kovchegov, N. Shulzhenko, K. L. Mine, X. Dong, A. Morgun, Unexpected links reflect the noise in networks. *Biol. Direct* **11**, 52 (2016). doi:10.1186/s13062-016-0155-0 Medline

43. P. Shannon, A. Markiel, O. Ozier, N. S. Baliga, J. T. Wang, D. Ramage, N. Amin, B. Schwikowski, T. Ideker, Cytoscape: A software environment for integrated models of biomolecular interaction networks. *Genome Res.* **13**, 2498–2504 (2003). doi:10.1101/gr.1239303 Medline

44. A. M. Bolger, M. Lohse, B. Usadel, Trimmomatic: A flexible trimmer for Illumina sequence data. *Bioinformatics* **30**, 2114–2120 (2014). doi:10.1093/bioinformatics/btu170 Medline

45. B. Langmead, S. L. Salzberg, Fast gapped-read alignment with Bowtie 2. *Nat. Methods* **9**, 357–359 (2012). doi:10.1038/nmeth.1923 Medline

46. D. Li, C. M. Liu, R. Luo, K. Sadakane, T. W. Lam, MEGAHIT: An ultra-fast single-node solution for large and complex metagenomics assembly via succinct de Bruijn graph. *Bioinformatics* **31**, 1674–1676 (2015). doi:10.1093/bioinformatics/btv033 Medline

47. D. E. Wood, J. Lu, B. Langmead, Improved metagenomic analysis with Kraken 2. *Genome Biol.* **20**, 257 (2019). doi:10.1186/s13059-019-1891-0 Medline

48. T. Seemann, Prokka: Rapid prokaryotic genome annotation. *Bioinformatics* **30**, 2068–2069 (2014). doi:10.1093/bioinformatics/btu153 Medline

49. Z. Gu, R. Eils, M. Schlesner, Complex heatmaps reveal patterns and correlations in multidimensional genomic data. *Bioinformatics* **32**, 2847–2849 (2016). doi:10.1093/bioinformatics/btw313 Medline

50. N. Segata, J. Izard, L. Waldron, D. Gevers, L. Miropolsky, W. S. Garrett, C. Huttenhower, Metagenomic biomarker discovery and explanation. *Genome Biol.* **12**, R60 (2011). doi:10.1186/gb-2011-12-6-r60 Medline

51. G. D. Bader, C. W. Hogue, An automated method for finding molecular complexes in large protein interaction networks. *BMC Bioinformatics* **4**, 2 (2003). doi:10.1186/1471-2105-4-2 Medline